RESEARCH ARTICLE OPEN ACCESS

Brainwide Projections of Mouse Dopaminergic Zona Incerta Neurons

Bianca S. Bono[1] | Kenichiro Negishi[2] | Yasmina Dumiaty[1] | Monica S. Ponce-Ruiz[2] | Titilayo C. Akinbode[1] | Kayla S. Baker[1] | C. Duncan P. Spencer[1] | Elizabeth Mejia[2] | Marina Guirguis[1] | Alex J. Hebert[1] | Arshad M. Khan[2,3] | Melissa J. Chee[1]

[1]Department of Neuroscience, Carleton University, Ottawa, Ontario, Canada | [2]Department of Biological Sciences, The University of Texas at El Paso, El Paso, Texas, USA | [3]Border Biomedical Research Center, The University of Texas at El Paso, El Paso, Texas, USA

Correspondence: Bianca S. Bono (biancabono@cmail.carleton.ca) | Melissa J. Chee (melissa.chee@carleton.ca)

ABSTRACT

The zona incerta (ZI) supports diverse behaviors including binge feeding, sleep–wake cycles, nociception, and hunting. Diverse ZI functions can be attributed to its heterogeneous neurochemical characterization, cytoarchitecture, and efferent connections. The ZI is predominantly GABAergic, but we recently identified a subset of medial ZI GABA cells that are marked by the enzyme tyrosine hydroxylase (TH) and produce dopamine (DA). While the role of GABA within the ZI is well studied, less is known about the functions of ZI DA cells. To identify potential roles of ZI DA cells, we further phenotyped them and mapped their efferent fiber projections. We showed that wild-type TH-immunoreactive (-ir) ZI cells did not express somatostatin or calretinin immunoreactivity. We next validated a *Th-cre;L10-Egfp* mouse line and found that medial *Egfp* ZI cells were more likely to be TH-ir. We therefore delivered a Cre-dependent virus into the medial ZI of *Th-cre* or *Th-cre;L10-Egfp* mice and selected two injection cases for full brain mapping, namely, cases with the lowest and highest colocalization between TH-ir and virally transduced, DsRed-labeled cells, to identify common target sites. Overall, DsRed-labeled fibers were distributed brainwide and were most prominent within the motor-related midbrain (MBmot), notably the periaqueductal gray area and superior colliculus. We also observed numerous DsRed-labeled fibers within the polymodal association cortex-related thalamus (DORpm), like paraventricular thalamic nucleus and nucleus of reunions, that processes external and internal sensory input. Overall, ZI DA cells displayed a similar fiber profile to ZI GABA cells and may integrate sensory input to coordinate motor output at their target sites.

Bianca S. Bono, Kenichiro Negishi, and Yasmina Dumiaty contributed equally to the manuscript.

Arshad M. Khan and Melissa J. Chee are joint senior authors.

1 | Introduction

The zona incerta (ZI), a subthalamic structure situated between the thalamus and hypothalamus, captured scientific interest because of its strategic position to important fiber systems in the human brain (Forel 1877; Malone 1910; Nauta and Haymaker 1969). Cajal (1911/1995) provided the first detailed drawings of mouse ZI neurons from Golgi-stained material and identified ascending medial lemniscal, bidirectional internal capsular, and descending corticothalamic fiber systems in close association with ZI cell populations that surmised sensorimotor communication roles for the ZI. Indeed, the ZI is currently being examined as a clinical target for movement disorders like Parkinson's disease (Blomstedt et al. 2018), as deep brain stimulation of the caudal ZI reduces muscle rigidity and tremors (Plaha et al. 2006, 2008). On the sensory side, functional neuroanatomical work in rat identified ZI importance in the paralemniscal pathway for conveying vibrissal, somatosensory information to the cortex, and this is distinct from medial lemniscal pathways contacting sensory thalamic structures (Diamond and Ahissar 2007; Urbain and Deschênes 2007). In addition to somatosensation, the ZI also integrates input from varied sensory modalities, including nociceptive (Masri et al. 2009; Moon and Park 2017), visual (Zhao et al. 2019), olfactory (Li et al. 2024), and auditory input (Shang et al. 2019; Li et al. 2024). Collectively, neuroanatomical and functional studies have defined the ZI as an important structure in sensorimotor processing and motor coordination, and the ZI is recognized as an integrative node that permits the organism to interact and respond to its environment (Wang et al. 2020b). For example, ZI activation is important for the integration of somatic, visual, and auditory functions during hunting (Zhao et al. 2019), and activating the ZI can suppress flight responses from a loud sound or suppress defensive behaviors (Chou et al. 2018).

Our understanding of the ZI has been refined by chemoarchitectural characterization across various taxa. The ZI predominantly comprises Gamma-aminobutyric acid (GABA) cells in mouse and other taxa (Lin et al. 1990; Yang et al. 2022), but the ZI produces other markers or chemical messengers, including somatostatin (Finley et al. 1981; Lin et al. 2023) and the LIM homeobox 6 (Lhx6) transcription factor (Liu et al. 2017) that likely contribute to its diverse behavioral and physiological functions. GABAergic ZI signaling is implicated in defensive behaviors (Chou et al. 2018), hunting (Zhao et al. 2019), feeding (Zhang and van den Pol 2017; Ye et al. 2023), as well as regulation of the sleep and wake cycle (Liu et al. 2017) and threat-induced escape (Lin et al. 2023). Such functional diversity implies role(s) for numerous target sites from ZI projections. A recent study confirmed that GABAergic ZI cells have widespread, brainwide projections (Yang et al. 2022), but it is not known if each ZI cell type contributes similarly or uniquely to the overall distribution of ZI projections.

We recently showed that a subset of GABAergic ZI cells was marked by the coexpression of tyrosine hydroxylase (TH) and contained dopamine (DA; Negishi et al. 2020), but ZI DA cells do not express a dopamine transporter (DAT; Sharma et al. 2018; Fougère et al. 2021), so DA signaling may be primarily regulated by DA synthesis and not extracellular reuptake. However, it is not clear if these GABAergic ZI DA neurons are part of existing peptidergic ZI cell types and where their specific targets are located.

In this study, we used a *Th-cre* transgenic mouse to trace and map the fiber projections of ZI DA cells using an anterograde, Cre-dependent viral tracer. We overlaid ZI DA fiber distribution patterns from two injection cases to delineate common projection targets and found that this GABAergic ZI DA population also projects widely throughout the brain. The distribution of *Th-cre* fibers overlapped with known targets of ZI neurons (Yang et al. 2022) and also within a refined subset of those targets. For example, fibers within motor-related midbrain regions were prominent only in the periaqueductal gray and superior colliculus, and fibers in the polymodal association cortex-related thalamus converged mainly in the paraventricular nucleus of the thalamus and nucleus of reuniens. We also showed that these ZI TH cells did not coexpress additional peptidergic ZI markers like somatostatin or calretinin, which suggested that GABAergic ZI DA cells represent a unique ZI subpopulation and may contribute to behaviors previously ascribed to ZI GABA cells, especially those requiring motor coordination, like hunting, defensive behaviors, and flight responses.

2 | Materials and Methods

2.1 | Subjects

All experimental procedures were performed in accordance with the Animal Care Committee at Carleton University. Mice were group-housed with a 12:12 h light–dark cycle (21–22°C) and provided water and standard rodent chow ad libitum (2014 Teklad, Envigo, Mississauga, Canada). To visualize TH neurons, the *Th-IRES-cre* (Lindeberg et al. 2004) mouse was crossed to a *R26-lox-STOP-lox-L10-Egfp* reporter mouse (Krashes et al. 2014) to produce *Th-cre;L10-Egfp* mice expressing enhanced green fluorescent protein (EGFP) under the *Th* promoter. All transgenic mice were backcrossed onto a C57/BL6J background (strain:000664, RRID:IMSR_JAX:000664; Jackson Laboratories, Bar Harbor, ME, USA).

2.2 | Antibody Characterization

The primary antibodies used for immunohistochemistry (IHC) are listed in Table 1.

Goat anti-somatostatin (D-20) antibody was raised against a synthetic peptide representing amino acids 84–102 of human somatostatin. Specificity of this antibody was confirmed by the absence of somatostatin immunoreactivity in somatostatin knockout mice (Lepousez et al. 2010).

Mouse anti-calretinin (H-5) antibody recognizes amino acids 2–27 of human calretinin. Specificity for this antibody was determined by performing a western blot in human and rat tissue (Santa Cruz Biotechnology).

Rabbit anti-DsRed antibody was raised against a variant of the *Discosoma* sp. red fluorescent protein and can label various red fluorescent proteins, including mCherry and tdTomato. Antibody specificity was demonstrated by the absence of immunostaining

TABLE 1 | Primary antibodies used for immunohistochemistry.

Antibody	Immunogen	Clonality, Isotype	Source, Catalog no., Lot no.	RRID	Titer
Goat anti-somatostatin (D-20)	Raised against synthetic peptide comprising amino acids 84–102 of human somatostatin	Polyclonal, IgG	Santa Cruz Biotechnology, sc-7819, F3014	AB_2302603	1:500
Mouse anti-calretinin (H-5)	Amino acids 2–27 of N-terminus of human calretinin	Monoclonal, $IgG_{2b}\,\kappa$	Santa Cruz Biotechnology, sc-365956, K1524	AB_10846469	1:500
Rabbit anti-dsRed	Full-length dsRed-Express	Polyclonal, IgG	Takara Bio USA, 632496, 1202020	AB_10013483	1:1000
Rabbit anti-NeuN	Recombinant mouse NeuN	Monoclonal IgG	Millipore Sigma, MABN140, 3792972	AB_2571567	1:2000
Rat anti-mCherry	Full-length mCherry protein	Monoclonal IgG2a	ThermoFisher Scientific, M11217, YL382780	AB_2536611	1:2000
Mouse anti-tyrosine hydroxylase	Purified from PC12 cells	Monoclonal, IgG	Millipore Sigma, MAB318, 2849094	AB_2201528	1:2000
Sheep anti-tyrosine hydroxylase	Purified from pheochromocytoma	Polyclonal, IgG	GeneTex, GTX82570, 822005648	AB_11177031	1:1000

in Cre-expressing tissues that do not produce tdTomato (Cheng et al. 2009; Chee et al. 2013).

Rabbit anti-NeuN antibody was raised against recombinant protein representing NeuN in a mouse. Specificity of this antibody has been confirmed in mouse brain tissue via western blot corresponding to bands at 46/48 kDa (Millipore, Burlington, MA, USA).

Rat anti-mCherry antibody was raised against the full-length mCherry protein. Specificity was determined via immunostaining in HEK-293 cells transfected with an mCherry-histone H3 construct, which revealed nuclear expression that was specific to only the transfected cells (ThermoFisher, Waltham, MA, USA). We confirmed that this antiserum produced no labeling in wild-type mice that lack this peptide (data not shown).

Mouse anti-TH antibody was produced from purified PC12 cells. Specificity of this antibody was determined by absence of labeling after unilateral lesioning of the ventral tegmental area (VTA) and substantia nigra in rats (Chung et al. 2008; Bourdy et al. 2014). Further specificity of this antibody has been shown in zebrafish, for which knocking out *Th1*, a gene that encodes TH in the central nervous system of zebrafish, abolishes TH immunoreactivity in the brain (Kuscha et al. 2012).

Sheep anti-TH antibody was produced by purification from pheochromocytomas. Specificity of this antibody was determined by lower TH-expressing cells in the substantia nigra following unilateral, 6-hydroxydopamine hydrobromide lesion to the rat striatum of rats (Choudhury et al. 2011).

The secondary antibodies used are listed in Table 2 and were raised in a donkey against the species of the corresponding primary antibody (i.e., rabbit, mouse, sheep).

2.3 | Stereotaxic Injections

Male (4–8-week old) *Th-cre* or *Th-cre;L10-Egfp* mice ($N = 7$) were administered meloxicam (5 mg/kg) analgesia subcutaneously (sc) and then secured in a stereotaxic frame (Kopf Instruments, Tujunga, CA, USA) under deep isoflurane anesthesia. Mice were unilaterally injected with 25–75 nL (25 nL/min) of a Cre-dependent adeno-associated virus (AAV) encoding mCherry (AAV8–EF1α–DIO–ChR2(H134R)–mCherry; 4.4×10^{12} genomic copies/mL, lot AAV2037, Canadian Neurophotonics Platform Viral Vector Core Facility [RRID:SCR_016477]) or tdTomato (AAV2/DJ–EF1α–DIO–ChETA–tdTomato; 1.7×10^{13} genomic copies/mL, lot AAV1131, Canadian Neurophotonics Platform) at the medial ZI using coordinates (in mm) relative to bregma at the skull surface: anteroposterior, −1.40 or −1.50; mediolateral, −0.50 or −0.70; dorsoventral, −4.70 (Paxinos and Franklin, 2004). Mice were allowed to recover for 4 weeks to promote viral transduction and reporter expression along nerve terminals.

2.4 | Tissue Processing

Brain tissue was prepared and collected as previously described (Bono et al. 2022), unless indicated otherwise, in the light phase

TABLE 2 | Secondary antibodies used for immunohistochemistry.

Antibody	Immunogen	Source, Catalog no., Lot no.	RRID	Titer
Biotin-conjugated donkey anti-rabbit	IgG (H + L)	Jackson ImmunoResearch, 711-065-152, 116529	AB_2340593	1:1000
Donkey anti-goat Alexa 594	IgG (H + L)	ThermoFisher A11058, 38472A	AB_2313737	1:500
Donkey anti-mouse Alexa 568	IgG (H + L)	Invitrogen, A10037, 1827879	AB_11180865	1:500
Donkey anti-mouse DyLight 649	IgG (H + L)	Jackson ImmunoResearch, 715-496-150[a], 82079	n/a[b]	1:500
Donkey anti-rabbit Cy 3	IgG (H + L)	Jackson ImmunoResearch, 711-166-152, 7456	AB_2313568	1:500
Donkey anti-rat Alexa 647	IgG (H + L)	Invitrogen, A78947, 2782618	AB_2910635	1:500
Donkey anti-sheep Alexa 488	IgG (H + L)	Invitrogen, A11015, 44695A	AB_141362	1:500
Donkey anti-sheep Cy 3	IgG (H + L)	Jackson ImmunoResearch, 713-165-147, 148268	AB_2315778	1:500

[a]This item has since been discontinued.
[b]Not available.

following transcardial perfusion with chilled (4°C) saline (0.9% NaCl) and then 10% formalin. Harvested brains were postfixed in 10% formalin for at least 12 h then cryoprotected in phosphate-buffered saline (PBS; pH 7.4, 0.01 M) containing 20% sucrose and 0.05% sodium azide for 18–24 h.

2.4.1 | In Situ Hybridization (ISH)

Brain tissue from male *Th-cre;L10-Egfp* mice ($n = $ 3, 8–10-week old) was collected in PBS and immediately mounted onto Superfrost Plus microscope slides (Fisher Scientific, Hampton, NH, USA). The slides were left to air-dry at room temperature (RT; 21–22°C) for 1 h, at −20°C overnight, and then packed into slide boxes for storage at −80°C.

2.4.2 | Injection Case Validation and Mapping

Brain tissue from male *Th-cre* or *Th-cre;L10-Egfp* mice was sliced into four series of 20–30 μm-thick sections and stored at −80°C in an antifreeze solution comprising 50% formalin, 20% glycerol, and 30% ethylene glycol. Tissues were later processed for indirect fluorescence or immunoperoxidase IHC.

2.5 | Nissl Staining

Brain tissues underwent Nissl staining as previously described (Negishi et al. 2020; Bono et al. 2022; Miller et al. 2024).

2.6 | Dual-Label ISH and IHC

Th-cre;L10-Egfp brain tissues underwent target retrieval and Protease III treatment as previously described (Bono et al. 2022). In brief, RNAscope probes (Table 3) *Mm-Ppib* for positive control targeting, *Bacillus dapB* for negative control targeting, or *Egfp-O2* and *Mm-Th* for experimental targeting were added to their respective slides and hybridized for 2 h at 40°C. *Egfp* and *Th* probes were added to probe diluent (1:50; 300041, Advanced Cell Diagnostics (ACD)) as neither probe occupied Channel 1. Probe detection was enhanced by amplifiers (AMP), and following AMP-mediated amplification (AMP1, AMP2, AMP3), the tissues were first treated with HRP-C2 (15 min, 40°C; 323105, ACD) to develop *Egfp* hybridization visualized with Opal 520 (FP1487001KT, PerkinElmer, Waltham, MA, USA) diluted in Tyramide Signal Amplification (TSA) buffer (1:750; 322809, ACD) and then with HRP-C3 (15 min, 40°C; 323106, ACD) to develop *Th* hybridization visualized with Opal 690 (FP1497001KT, Perkin Elmer) diluted in TSA buffer (1:750).

TABLE 3 | List of RNAscope probes for in situ hybridization.

Probe	Protein	Z pairs	Target (bp)	Catalog no.	Accession ID
Mm-Egfp	Enhanced green fluorescent protein	13	628–1352	556431-C2	U55763.1
Mm-Th	Tyrosine hydroxylase	20	483–1063	317621-C3	NM_009377.1
dapB	Dihydrodipicolinate reductase	10	414–862	310043	EF191515
Ppib	Peptidylprolyl isomerase B	15	98–856	313911	NM_011149.2

After ISH treatment, tissues were processed for IHC as previously described (Bono et al. 2022). In brief, the tissues were incubated with a sheep anti-TH (1:1000; diluted in PBS) for 30 min at RT (23°C) and then a donkey anti-sheep Cyanine (Cy) 3 (1:500; diluted in PBS) for 30 min (RT).

2.7 | Indirect Fluorescence IHC

All tissues were blocked with 3% normal donkey serum and underwent IHC processing as previously described (Shammah-Lagnado et al. 1985; Chee et al. 2013; Tapia et al. 2023). To determine the neurochemical composition of TH-immunoreactive (-ir) cells, free-floating brain sections were incubated with sheep anti-TH (1:1000) and mouse anti-calretinin (1:500) primary antibodies or mouse anti-TH (1:1000) and goat anti-somatostatin for 24 h (RT). After washing, the sections were then incubated with a donkey anti-sheep-conjugated Alexa Fluor 488 (1:500) with donkey anti-mouse-conjugated Alexa Fluor 568 (1:500) secondary antibodies (2 h, RT) or donkey anti-mouse Alexa Fluor 488 with donkey anti-goat Alexa Fluor 594 secondary antibodies (2 h, RT), respectively.

To determine viral spread at the injection site and the extent of viral transduction at TH-ir cells, brain sections were incubated with rabbit anti-DsRed (1:1000) and mouse anti-TH (1:2000) primary antibodies (24 h, RT) followed with donkey anti-rabbit Cy 3 (1:500) and donkey anti-mouse DyLight 649 (1:500) secondary antibodies.

To confirm that virus-transfected fibers contacted neurons, we incubated sections with rat anti-mCherry (1:2000) and rabbit anti-NeuN (1:2000) primary antibodies (24 h, RT) followed by donkey anti-rat Alexa 647 (1:500) and donkey anti-rabbit Cy 3 (1:500) secondary antibodies.

2.8 | Indirect Immunoperoxidase IHC

As previously described (Chee et al. 2013), injection cases selected for fiber mapping underwent IHC processing with an immunoperoxidase reaction to enhance labeling of virally transduced *Th-cre* fiber projections. In brief, free-floating brain sections were placed in a blocking solution containing 3% normal donkey serum for 2 h (Jackson ImmunoResearch Laboratories, Inc., West Grove, PA, USA) and then incubated with rabbit anti-DsRed primary antibody (1:1000) for 24–48 h at 4°C and then a biotin-conjugated donkey anti-rabbit secondary antibody (1:1000) for 5 h (RT). After rinsing in five 5-min exchanges of Tris-buffered saline (TBS; RT), the sections were treated to form avidin–biotin horseradish peroxidase complexes (ABC) at biotin-conjugated sites using the Vectastain Elite ABC kit (0.45% v/v Reagent A and B in TBS containing 0.1% Triton X-100; PK-6100, Vector Laboratories) for 1 h (RT). Ds-Red immunoreactivity was then developed by reacting the sections in a 0.05% 3,3′-diaminobenzidine (DAB) and 0.015% hydrogen peroxide TBS cocktail for 15–20 min (RT). Finally, the sections were washed in five 5-min exchanges of TBS and mounted onto gelatin-coated slides. After air-drying, the slides were dehydrated in ascending concentrations of ethanol (50%, 70%, 95%, and 100% × 3 for 3 min each), delipidated in xylene (25 min), and coverslipped with dibutylphthalate polystyrene xylene (DPX) mountant (06522, Sigma Aldrich, St. Louis, MO, USA).

2.9 | Microscopy

2.9.1 | Brightfield Imaging

Large field-of-view photomicrographs of Nissl-stained brain sections were acquired via a Plan Apochromat ×4 objective lens (0.20 numerical aperture) mounted on a Nikon Eclipse Ti2 inverted microscope (Nikon Instruments Inc., Mississauga, Canada) equipped with a fully motorized stage and DS-Ri2 color camera (Nikon) as previously described (Negishi et al. 2020; Bono et al. 2022). To differentiate between axon fibers and terminals, high-magnification photomicrographs were acquired via a ×40 objective lens (0.95 numerical aperture).

2.9.2 | Epifluorescence Imaging

Large field-of-view photomicrographs of DAPI-stained nuclei or DsRed-ir cells were acquired using a Prime 95B CMOS camera (Photometrics, Tucson, AZ, USA). DAPI- or Cy3-labeled excitation was provided by a SPECTRA X light engine (Lumencor, Beaverton, OR, USA) passing through an ET395/25x or ET550/15x excitation filter (Chroma Technology Corporation, Bellows Falls, VT, USA), respectively.

2.9.3 | Confocal Imaging

High-magnification photomicrographs were generated using a Nikon C2 confocal system fitted with a Plan Apochromat ×10 objective lens (0.45 numerical aperture). Regions of interest were identified by epifluorescence imaging (as described in 2.9.2).

To analyze ISH-treated tissue, photomicrographs were generated with 405-, 488-, 561-, and 640-nm wavelength lasers to visualize

4',6-diamidino-2-phenylindole- (DAPI), Opal 520-, Opal 690-, and Cy 3-labeled signals, which were pseudocolored dark blue, green, magenta, and light blue, respectively. The same image acquisition settings were used to acquire images from experimental tissue, *dapB*-treated negative control tissue, and *Ppib*-treated positive control tissue. Photomicrographs from experimental tissue were adjusted using the same image processing settings applied to photomicrographs captured from *dapB*-hybridized tissues until no fluorescence was visible (Bono et al. 2022); this subtracted the background or fluorescence arising from nonspecific binding.

To determine the colocalization of TH-immunoreactivity with calretinin or somatostatin, confocal photomicrographs were generated with 488- and 561-nm wavelength lasers to visualize Alexa Fluor 488- and Alexa Fluor 568-labeled signals, which were pseudocolored green and magenta, respectively. To analyze the spread of the injection site, confocal photomicrographs were generated with 561- and 640-nm wavelength lasers to visualize Cy 3- and DyLight 649-labeled signals, which were pseudocolored red and light blue, respectively.

Fiber appositions at target somata were assessed as previously described (Payant et al. 2024). In brief, *z*-stacks were acquired with a Plan Apochromat ×40 objective lens (0.95 numerical aperture) using 561- and 640-nm wavelength lasers to visualize Cy 3- and Alexa Fluor 647-labeled signals, which were pseudocolored white and red, respectively. *Z*-stack sections were displayed as orthogonal *xy*, *xz*, and *yz* projections (NIS-Elements Imaging Software) and appositions were defined when there was no discernible space between the fiber and soma along the *xz* and *yz* projections (Krimer et al. 1997; Lambe et al. 2000; Bouyer and Simerly 2013).

2.9.4 | Darkfield Imaging

Wide-field photomicrographs of DAB-stained sections were acquired with a ×10 objective lens (0.40 numerical aperture) mounted on an Olympus BX-63 microscope (Olympus Corporation, Tokyo, Japan) fitted with a darkfield condenser, motorized stage, and DP74 color camera. Tiled images were stitched and adjusted with cellSens Dimension imaging software (Version 2.3, Olympus) and exported as TIFF files.

2.10 | Image and Fiber Analysis

All photomicrographs generated were tiled and stitched using NIS-Elements (Nikon Corporation, Konan, Japan), unless otherwise indicated. Any adjustments to the brightness, intensity, or contrast were applied to the entire photomicrograph via NIS-Elements and then the photomicrographs were exported as TIFF files in Illustrator 2023 (Adobe Inc., San Jose, CA, USA). Any additional text, labels, or symbols (e.g., arrowheads or outlines) were added in Illustrator 2023.

2.10.1 | Plane-of-Section Analysis

Nissl-based parcellations were determined as previously described (Negishi et al. 2020; Bono et al. 2022).

2.10.2 | Atlas-Based Mapping

Nissl-based parcellations were transferred to large field-of-view epifluorescence images, which were aligned to their corresponding Nissl photomicrographs. The corresponding high-magnification confocal photomicrographs were then aligned to the epifluorescence photomicrographs for either cell counting or fiber tracing. Cell bodies were labeled using the *Paintbrush* tool, and fibers were traced using the *Pen* tool (Illustrator 2023, Adobe). The labeled cell bodies or traced fibers were then transferred onto the corresponding *Allen Reference Atlas* (*ARA*) template (Dong 2008). Differences in plane-of-section mediolaterally or dorsoventrally within a brain slice were carefully assessed so that angular differences in any dimension prompted a fragmented approach when mapping onto atlas templates (Simmons and Swanson 2009).

2.10.3 | Quantification of ISH Cells

Both *Egfp* and *Th* hybridization appeared as clusters of punctate "dots," and *Egfp*- or *Th*-hybridized cells were marked using the *Blob Brush* tool in Illustrator if it expressed three or more dots per cell and if these dots localized to a 4',6-diamidino-2-phenylindole (DAPI)-stained soma. Only cell counts at *ARA* levels (L) that were available from at least two brains were included in our dataset. As previously described, cell counts were corrected for oversampling using the Abercrombie formula (Negishi et al. 2020; Bono et al. 2022), where mean tissue thickness (25.31 µm) was determined from 15 hypothalamic brain sections and mean cell diameter (12.82 µm) was determined from 50 cell profiles within the ZI.

2.10.4 | Quantification of DsRed-Labeled Fibers

Each brain region was grouped into one of 20 subdivisions that we formed based on the hierarchical organization scheme (Wang et al. 2020a) and ontology (Allen Institute for Brain Science 2011) provided by the *ARA* (Supporting Information Figure 1). Large-scale quantification of DsRed-labeled fibers was determined from manual fiber tracings that were mapped onto *ARA* templates and then analyzed by each major brain division, which included: isocortex; olfactory regions of the cortex; hippocampal formation; cortical subplate of the cerebral cortex; striatum; palladium; sensory–motor- and polymodal cortex-related regions of the thalamus; periventricular zone, periventricular region, medial zone, and lateral zone of the hypothalamus; sensory, motor, and behavioral-state-related regions of the midbrain; and sensory-motor, and behavioral-state-related regions of the pons. Mapped fiber tracings from each major brain division were transferred to Photoshop 2023 (Adobe) to determine the density of fibers in the whole brain division per *ARA* level.

Fiber coverage was determined in each region of interest by first using the *Lasso* tool to outline the borders of the region. Using the *Histogram* panel, we then selected "entire image" under the *Source* dropdown menu to obtain the total number of pixels within the outlined region; this determined the total region area. Next, we adjusted the *Source* menu to "selected layer" that contained the traced fibers to obtain the number of pixels occupied by a traced fiber.

2.10.5 | Intersecting Fibers Maps

Fiber maps from two injection cases were overlaid in separate layers using Illustrator 2023 (Adobe). The traced fibers from each injection case were converted into compound paths, and the compound paths from each injection case were overlaid upon one another. Compound paths that overlapped and mapped to the same region in both injection cases were identified using the *Intersect Pathfinder* tool in the *Pathfinder panel*.

2.11 | Statistics

Statistical analyses and accompanying graphs were generated using GraphPad Prism 7 (GraphPad Software Inc., San Diego, CA, USA). A Pearson correlation coefficient with 95% confidence intervals was applied to correlate fiber coverage between injection cases and between the intersecting fiber coverage and the total region area. Likewise, a two-way analysis of variance (ANOVA) with Tukey's Honestly Significant Difference (HSD) was performed to identify differences in the percentage of EGFP+ cell types within the medial and lateral ZI. Statistical significance was determined at $p < 0.05$. All data are presented as mean $\pm$ standard error of the mean (*SEM*).

3 | Results

3.1 | TH ZI Cells Lacked Additional Neurochemical ZI Markers

We previously showed that GABAergic TH ZI cells do not produce additional neuropeptides like melanin-concentrating hormone or hypocretin/orexin that are associated with the ZI (Negishi et al. 2020). To further assess if ZI TH cells may represent a unique ZI subpopulation, we determined if TH ZI cells colocalized with known ZI markers like somatostatin (Kolmac and Mitrofanis 1999) and calretinin (Li et al. 2021). Somatostatin- (Figure 1a,b) and calretinin-ir (Figure 1c,d) cells were adjacent to or interspersed among TH-ir cells in the medial ZI. However, medially distributed TH ZI cells did not coexpress somatostatin (Figure 1a,b) or calretinin immunoreactivity (Figure 1c,d), thus indicating that TH ZI cells represented a ZI subpopulation unique from these phenotypes.

3.2 | Validation of *Th-cre* Expression in the ZI

We evaluated the efficacy and specificity of Cre-mediated expression at the ZI of *Th-cre;L10-Egfp* mice ($N = 3$) by determining the colocalization of *Th* mRNA and TH immunoreactivity in cells expressing *Egfp* mRNA. *Egfp*-hybridized cells in the ZI spanned levels (L) 60–71 of the *ARA* (Dong 2008), but they were most abundant at L67–69 (Figure 2a).

The vast majority (92 ± 4%) of *Egfp* ZI cells expressed *Th* mRNA, and only a few ZI cells (< 1%) that expressed *Th* mRNA were not *Egfp*-labeled. Interestingly, only 27 ± 5% of *Th*-expressing *Egfp* cells also expressed TH immunoreactivity, and these TH-ir cells predominantly clustered within L67–69 only and were typically medial to a parcelled cell cluster named "da" within the ZI
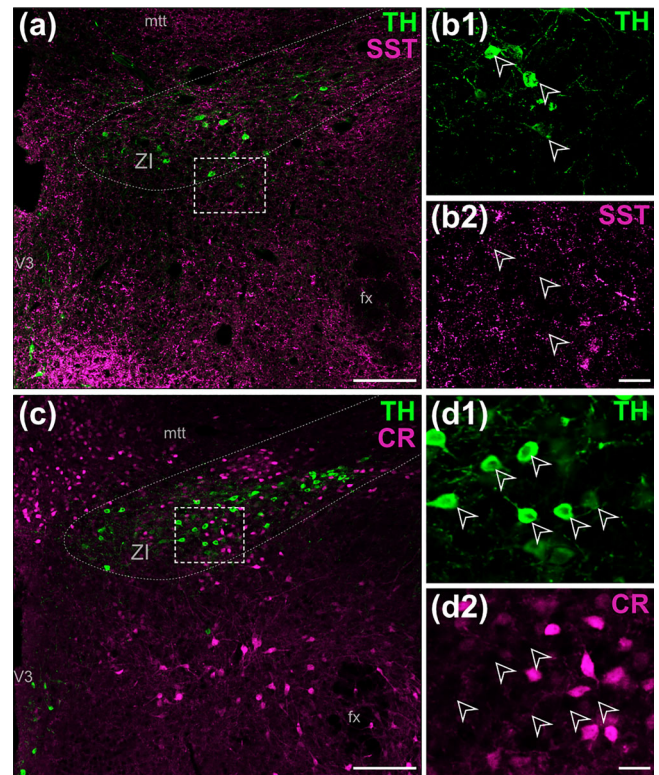
FIGURE 1 | Absence of somatostatin or claretinin immunoreactivity at ZI cells expressing tyrosine hydroxylase (TH) colocalization. Representative confocal photomicrographs of the wild-type ZI expressing TH and somatostatin (SST; a, b) or calretinin (CR; c, d) immunoreactivity. Single-channel confocal photomicrographs from the respective dashed outlined areas showing the lack of colocalization (open arrowheads) between TH (b1, d1) and somatostatin (b2) or calretinin (d2) immunoreactivity. Scale bars: 50 μm (a, c); 20 μm (b; d). fx, fornix; mtt, mammillothalamic tract; V3, third ventricle; ZI, zona incerta.

(Figure 2a,b). Furthermore, TH-ir, *Th*-, and *Egfp*-hybridized cells tended to be medially distributed within the ZI (Figure 2b). However, since we could not discern a Nissl-defined cytoarchitectural boundary within the ZI, we defined the medial and lateral ZI by a border along the lateral edge of the mammillothalamic tract and fornix (Figure 2c). The proportion of *Th*-hybridized *Egfp* cells were comparable between the medial (59 ± 5%; Figure 2d1,d2) and lateral ZI (41 ± 5%; $p = 0.227$; Figure 2e1,e2), but strikingly, the proportion of *Th*- and *Egfp*-hybridized cells that expressed TH immunoreactivity was significantly greater in the medial ZI (41 ± 8%; Figure 2f1) than lateral ZI (3 ± 0.4%; $p = 0.035$; Figure 2f2). Some ectopic *Egfp* cells (8 ± 3%) did not express either *Th* mRNA or TH immunoreactivity and were similarly scattered within the medial (3 ± 1%; Figure 2f1) and lateral ZI (14 ± 6%; $p = 0.156$; Figure 2f2).

3.3 | Injection Cases at Medial ZI May Contain Low or High TH Immunoreactivity

As *Th-cre* cells coexpressing TH-immunoreactivity were more prominent in the medial ZI, we delivered a Cre-dependent viral tracer encoding mCherry into the medial ZI of *Th-cre* or *Th-cre;L10-Egfp* mice ($N = 7$) in order to map the fiber projec-

FIGURE 2 | Robust colocalization of *Egfp* hybridization, *Th* hybridization, and tyrosine hydroxylase (TH) immunoreactivity in the medial zona incerta (ZI). Number (a) and spatial distribution of *Egfp* mRNA cells (b) that coexpressed TH immunoreactivity (dark 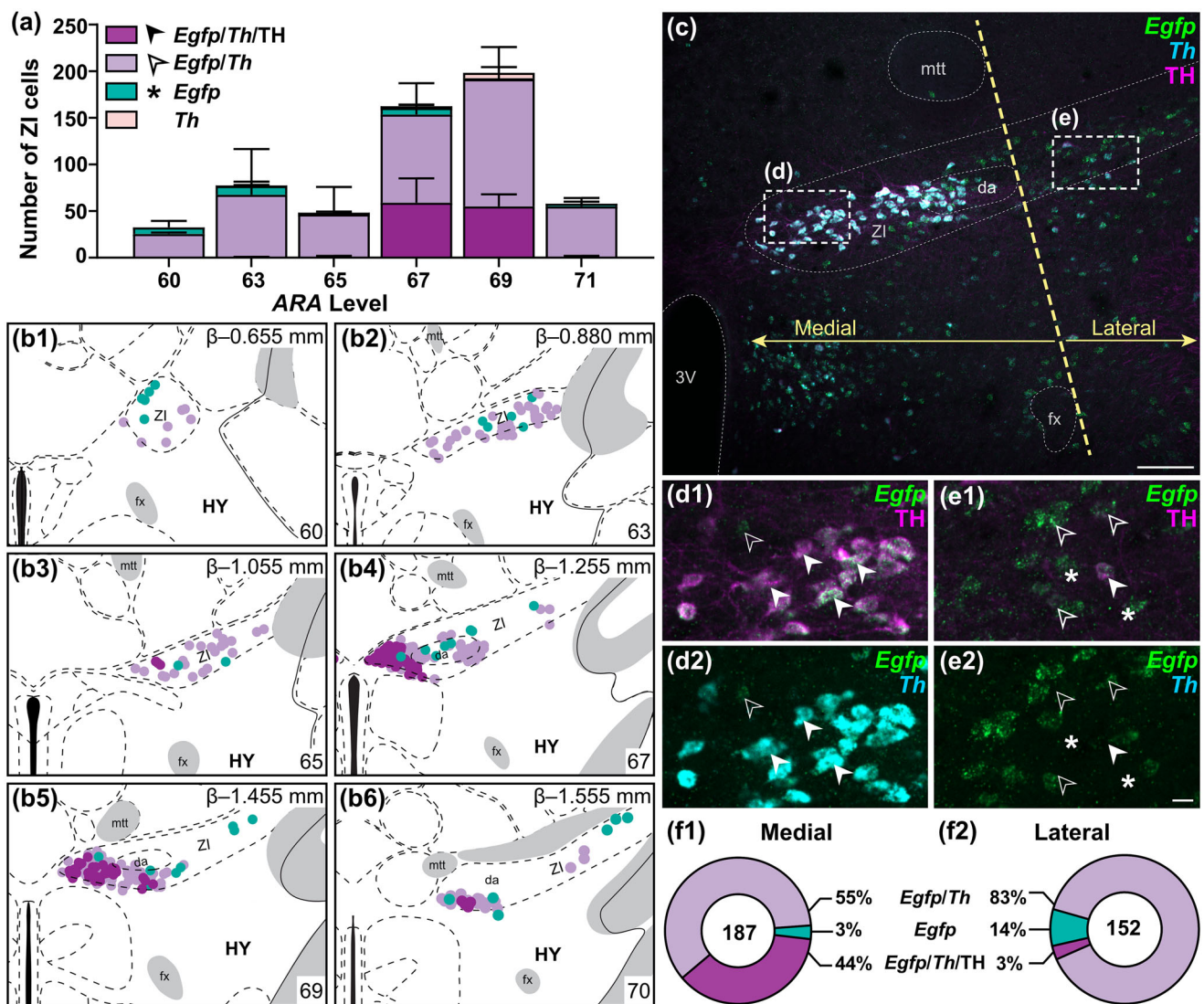purple) and/or *Th* hybridization (light purple) or that were ectopic and did not express either TH or *Th* (green) throughout the anteroposterior extent of the ZI in a *Th-cre;L10-Egfp* mouse (*N* = 3). Representative photomicrograph of the division between the medial and lateral ZI (yellow dashed line), which was defined by the lateral edge of the mammillothalamic tract (mtt) and fornix (fx; c). High-magnification photomicrographs (from dashed outlined area in c) of *Egfp*-expressing cells that were ectopic (asterisk) or that coexpressed TH immunoreactivity (closed arrowheads; 1) and/or *Th* hybridization (open arrowheads; 2) within the medial (d) or lateral ZI (e). Proportion of *Egfp* cells in the medial (1) and lateral ZI (2) that expressed *Th* mRNA or TH immunoreactivity (f). The numeral inside the donut chart indicates the average number of cells counted within the ZI. Average cell counts and maps at each *Allen Reference Atlas* (*ARA*) level are based on at least two brains. Maps were produced using *ARA* templates (Dong 2008) with reference to cytoarchitectural boundaries on Nissl-stained tissue. Panels with maps include the corresponding atlas level (bottom right), bregma (β; top right), and brain region labels using formal nomenclature from the *ARA*. Scale bar: 50 μm (c); 20 μm (d, e). 3 V, third ventricle; da, dopaminergic A13 group (nomenclature assigned by *ARA*).

tions from putative ZI DA cells, which were labeled by DsRed immunoreactivity. Importantly, when injected into *Th-cre;L10-Egfp* mice, all DsRed-ir cells colocalized with EGFP (Figure 3a,b) thus indicating the specificity of DsRed expression for *Th-cre* cells. To determine if TH-ir cells in the medial ZI contributed unique fiber projections, we selected one injection case each (i.e., Cases 1 and 7) that labeled a high versus low proportion of TH-ir DsRed-labeled cells (Table 4). Overall, about 70% of virally transduced DsRed-ir cells were constrained to the ZI, but we excluded cases where less than 50 DsRed-ir cells were labeled per brain series (i.e., Cases 4, 5, and 6). We prioritized injection cases

with a higher number of *Th-cre* cells transduced, thus we mapped and compared Case 1 and Case 7, which reflected cases with the lowest (17%) and highest (53%) percentage of TH-ir DsRed-labeled cells, respectively (Table 4).

3.4 | Mapping Intersecting Points to Define Common Spatial Targets of ZI *Th-cre* Cells

We mapped DsRed-labeled fibers from Case 1 and Case 7 onto *ARA* brain atlas templates (Dong 2008) and recorded the amount

TABLE 4 | List of injection cases at zona incerta (ZI) *Th-cre* cells.

Case	*ARA* range[b]	DsRed-ir cells[c]		TH-ir colocalization[e]
		Total	**ZI[d]**	
1	65–71	132	68%	17%
2	63–67	69	95%	50%
3	63–69	76	70%	47%
4	63–69	18	100%	33%
5	62–70	35	85%	51%
6	62–75	41	89%	37%
7	65–75	86	85%	53%

[a]Atlas levels defined by *Allen Reference Atlas* (*ARA*) templates (Dong 2008).

[b]Virally transduced DsRed-immunoreactive (-ir) cells counted unilaterally from one of four brain series sliced per brain.

[c]Percent of DsRed-ir cells constrained to the ZI.

[d]Percent of DsRed-ir cells that coexpress tyrosine hydroxylase (TH) immunoreactivity.

of fiber coverage, which we depicted in pixels, across the major divisions of the brain (Wang et al. 2020a; Allen Institute for Brain Science 2011). The fiber coverage within each brain division was strongly correlated between Case 1 and Case 7 ($r = 0.994$; $p < 0.0001$; Figure 4a), thus we overlaid the mapped fiber distribution from Case 1 and Case 7 to determine their points of intersection to define common spatial targets of medial ZI *Th-cre* cells.

Our intersecting analysis focused on *ARA* levels that spanned between +0.750 mm and −4.380 mm from bregma (L44–97) and on the hemisphere ipsilateral to the injection site where most DsRed-ir fibers were distributed (Figure 4b). Rostrally, DsRed-ir fibers appeared anterior to the genu of the corpus callosum (L47; +0.750 mm from bregma) and extended caudally into the posterior hindbrain. Unfortunately, sections caudal to L97 were not collected for Case 1, so DsRed-labeled fibers posterior to L97 were mapped from Case 7 only.

DsRed-ir fibers were largely restricted to subcortical structures in the thalamus, hypothalamus, and medulla (Figure 4c). Expectedly, we found strong DsRed labeling in the hypothalamic medial (MEZ) and lateral zone (LZ) where the injection site was localized. The polymodal association cortex-related thalamus (DORpm) and motor-related midbrain (MBmot) contained the greatest fiber coverage among major brain divisions away from the injection site (Figure 4c). Outside of the injection site, we considered whether the abundance of DsRed-labeled fibers in the DORpm and MBmot was related to the size of these brain divisions, but we found that the prevalence of fibers in a region was not related to the brain area ($r = 0.106$; $p = 0.676$; Figure 4d). Large brain divisions like the isocortex and striatum comprised only few DsRed-ir fibers, thus smaller brain divisions like the DORpm and MBmot that comprised high intersecting fiber coverage were especially notable (Figure 4d).

3.5 | Mapping Brainwide *Th-cre* Fiber Projections

The distribution patterns of DsRed-ir fibers were highly comparable between cases across all major brain divisions and most individual brain regions (Figure 5). We used a density scale (+++, high; ++, moderate; +, low; −, very low or none) to report semiquantitative estimates of fiber distribution in each brain region (Figure 6), and we provided a comprehensive summary of the projection patterns across all major brain divisions using the hierarchical structure (Wang et al. 2020a) and nomenclature (Allen Institute for Brain Science 2011), set forth by the *ARA*, for each injection case in Table 5. Where possible, we noted fibers that presented themselves in a continuous line or as clusters (Figure 7a,b). We then determined whether these fiber morphologies corresponded with appositions onto NeuN-labeled cell bodies or if they may represent fibers-of-passage (Figure 7c). DsRed-ir fibers appearing as clusters consistently formed appositions onto NeuN-labeled cell bodies (Figure 7d1). By contrast, most DsRed-ir fibers appearing as continuous lines occasionally formed appositions onto NeuN-labeled cell bodies (Figure 7d2), but the majority did not (Figure 7d3). We provide side-by-side comparisons of the distribution of DsRed-ir fibers from Case 1 (Figure 8a1–ff1), Case 7 (Figure 8a2–ff2), and their points of intersection (Figure 8a3–ff3) across all levels available in our dataset.

3.5.1 | Cerebral Cortex

DsRed-labeled fibers within the cerebral cortex were sparse relative to all other major brain divisions analyzed (Table 5).

3.5.1.1 | Cortical Plate (CTXpl). Subregions within the CTXpl including the isocortex, olfactory areas, and hippocampal formation contained few fibers. Although limited, fibers were observed in regions comprising olfactory areas, including the lateral olfactory tract (NLOT; Figure 8g–j), cortical amygdalar area (COA; Figure 8e–w), and piriform-amygdalar area (PAA; Figure 8k–t). However, this may not be reflected in the intersecting maps due to their sparsity (Table 5). The remaining olfactory areas, which included the piriform area (PIR; Figure 8a–u), PAA (Figure 8k–t), postpiriform transition area (TR; Figure 8t–y), main olfactory bulb (MOB), anterior olfactory nucleus (AON), tenia tecta (TT), and dorsal peduncular area (DP), were completely devoid of fibers (Table 5). Case 1 also revealed no fibers in

TABLE 5 | Qualitative distribution of fiber projections from zona incerta (ZI) *Th-cre* cells.

Major brain division[a]	Region[b] Subregion	Density of fiber coverage[c]		
		Case 1	Case 7	Intersect
Cortical plate				
Isocortex [ISO][d]		−	−	−
Olfactory areas [OLF]				
Main olfactory bulb	MOB	−	−	−
Accessory olfactory bulb	AOB	n/a	−	n/a
Anterior olfactory nucleus	AON	−	−	−
Tenia tecta	TT	−	−	−
Dorsal peduncular area	DP	−	−	−
Piriform area	PIR	−	−	−
Nucleus of the lateral olfactory tract	NLOT	+	+	+
Cortical amygdalar area	COA	+	+	−
Piriform-amygdalar area	PAA	−	+	−
Postpiriform transition area	TR	−	−	−
Hippocampal formation [HPF]				
Hippocampal region	HIP			
Ammon's horn	CA	+	+	−
Dentate gyrus	DG	−	−	−
Fasciola cinerea	FC	−	−	−
Induseum griseum	IG	−	−	−
Retrohippocampal region	RHP			
Enterohinal area	ENT	−	−	−
Parasubiculum	PAR	−	−	−
Postsubiculum	POST	−	−	−
Presubiculum	PRE	−	−	−
Subiculum	SUB	+	+	−
Cortical subplate [CTXsp]				
Claustrum	CLA	−	−	−
Endopiriform nucleus	EP	−	−	−
Lateral amygdalar nucleus	LA	−	−	−
Basolateral amygdalar nucleus	BLA	+	+	−
Basomedial amygdalar nucleus	BMA	+	+	−
Posterior amygdalar nucleus	PA	−	−	−
Cerebral nuclei				
Striatum [STR]				
Striatum, dorsal region	STRd	−	−	−
Striatum, ventral region	STRv	+	+	−
Lateral septal complex	LSX	++	+++	++
Striatum-like amygdalar region	sAMY	+	+	−
Pallidum [PAL]				
Pallidum, dorsal region	PALd	+	+	−
Pallidum, ventral region	PALv	++	++	+
Pallidum, medial region	PALm	+	++	+
Pallidum, caudal region	PALc	++	++	++

(Continues)

TABLE 5 | (Continued)

Major brain division[a]	Region[b] Subregion	Density of fiber coverage[c]		
		Case 1	Case 7	Intersect
Thalamus				
Sensory–motor cortex related [DORsm]				
Ventral group of the dorsal thalamus	VENT			
Ventral anterior–lateral complex	VAL	−	+	−
Ventral medial nucleus	VM	++	+++	++
Ventral posterior complex	VP	+	+	+
Subparafascicular nucleus	SPF	+++	+++	+++
Subparafascicular area	SPA	+++	+++	+++
Peripeduncular nucleus	PP	+++	++	++
Geniculate group, dorsal thalamus	GENd			
Medial geniculate complex	MG	+	+	+
Dorsal part of lateral geniculate complex	LGd	+	+	+
Polymodal association cortex related [DORpm]				
Lateral group of dorsal thalamus	LAT			
Lateral posterior nucleus	LP	++	++	++
Posterior complex	PO	+	+	−
Posterior limiting nucleus	POL	++	+	−
Supergeniculate nucleus	SGN	+	+	−
Anterior group of dorsal thalamus	ATN			
Anteroventral nucleus	AV	++	+	+
Anteromedial nucleus	AM	+	+	+
Anterodorsal nucleus	AD	+	++	+
Interanteromedial nucleus	IAM	++	++	+
Interanterodorsal nucleus	IAD	+	+	−
Lateral dorsal nucleus	LD	+	++	+
Medial group of dorsal thalamus	MED			
Intermediodorsal nucleus	IMD	+	+	+
Mediodorsal nucleus	MD	+	+	+
Submedial nucleus	SMT	++	++	+
Perireunesis nucleus	PR	++	+	+
Midline group of dorsal thalamus	MTN			
Paraventricular nucleus	PVT	+++	+++	++
Parataenial nucleus	PT	+++	+++	+++
Nucleus of reuniens	RE	+++	+++	++
Intralaminar nuclei of dorsal thalamus	ILM			
Rhomboid nucleus	RH	++	++	+
Central medial nucleus	CM	++	++	++
Paracentral nucleus	PCN	+	+	−
Central lateral nucleus	CL	++	++	++
Parafascicular nucleus	PF	+	+	+
Reticular nucleus	RT	+	+	+
Geniculate group of ventral thalamus	GENv			

(Continues)

TABLE 5 | (Continued)

Major brain division[a]	Region[b] Subregion	Density of fiber coverage[c]		
		Case 1	Case 7	Intersect
Intergeniculate leaflet of lateral geniculate complex	IGL	++	++	++
Ventral part of lateral geniculate complex	LGv	++	++	++
Subgeniculate nucleus	SubG	+	−	−
Epithalamus	EPI			
Medial habenula	MH	+	+	−
Lateral habenula	LH	++	++	++
Hypothalamus				
Periventricular zone [PVZ]				
Supraoptic nucleus	SO	++	+++	++
Paraventricular hypothalamic nucleus	PVH			
Magnocellular division	PVHm	+++	+++	+++
Parvicellular division	PVHp	+++	+++	+++
Periventricular hypothalamic nucleus, anterior part	PVa	+	+	+
Periventricular hypothalamic nucleus, intermediate part	PVi	++	+++	++
Arcuate hypothalamic nucleus	ARH	++	+++	++
Periventricular region [PVR]				
Anterodorsal preoptic nucleus	ADP	+	+	+
Anteroventral preoptic nucleus	AVP	+	++	+
Anteroventral periventricular nucleus	AVPV	+	+	+
Dorsomedial nucleus of the hypothalamus	DMH	+++	+++	+++
Median preoptic nucleus	MEPO	+	+	+
Medial preoptic area	MPO	++	++	++
Vascular organ of lamina terminalis	OV	−	−	−
Posterodorsal preoptic nucleus	PD[e]	n/a	n/a	n/a
Parastrial nucleus	PS	+	+	−
Periventricular hypothalamic nucleus, posterior part	PVp	++	+++	+
Periventricular hypothalamic nucleus, preoptic part	PVpo	++	++	+
Subparaventricular zone	SBPV	+++	+++	+++
Suprachiasmatic nucleus	SCH	+	+	+
Subfornical organ	SFO	−	−	−
Ventrolateral preoptic nucleus	VLPO	+	++	+
Hypothalamic medial zone [MEZ]				
Anterior hypothalamic nucleus	AHN	+++	+++	+++
Mammillary body	MBO	++	++	+
Medial preoptic nucleus	MPN	++	++	+
Dorsal premammillary nucleus	PMd	++	++	++
Ventral premammillary nucleus	PMv	+	++	+
Paraventricular hypothalamic nucleus	PVHd	+++	+++	+++
Ventromedial hypothalamic nucleus	VMH	++	+++	++
Posterior hypothalamic nucleus	PH	+++	+++	+++
Hypothalamic lateral zone [LZ]				
Lateral hypothalamic area	LHA	++	++	++
Lateral preoptic area	LPO	++	++	++

(Continues)

TABLE 5 | (Continued)

Major brain division[a]	Region[b] Subregion	Density of fiber coverage[c] Case 1	Case 7	Intersect
Preparasubthalamic nucleus	PST	++	++	+
Parasubthalamic nucleus	PSTN	++	++	++
Retrochiasmatic area	RCH	++	++	++
Subthalamic nucleus	STN	+	+	+
Tuberal nucleus	TU	++	++	++
Zona incerta	ZI	+++	+++	+++
Median eminence [ME]		−	++	−
Midbrain				
Midbrain, sensory related [MBsen]				
Superior colliculus, sensory related	SCs	++	++	+
Inferior colliculus	IC	++	++	++
Nucleus of brachium of inferior colliculus	NB	++	+	−
Nucleus sagulum	SAG	+	+	−
Parabigeminal nucleus	PBG	+	+	−
Midbrain trigeminal nucleus	MEV	n/a	+++	n/a
Midbrain, motor related [MBmot]				
Substantia nigra, reticular part	SNr	−	−	−
Ventral tegmental area	VTA	++	++	+
Midbrain reticular nucleus, retrorubral area	RR	++	++	+
Midbrain reticular nucleus	MRN	++	++	+
Superior colliculus, motor related	SCm	++	++	++
Periaqueductal gray	PAG	+++	+++	+++
Pretectal region	PRT	+	+	−
Cuneiform nucleus	CUN		++	
Red nucleus	RN	+	+	+
Oculomotor nucleus	III	−	−	−
Edinger–Westphal nucleus	EW	++	++	+
Trochlear nucleus	IV	−	−	−
Ventral tegmental nucleus	VTN	n/a	−	n/a
Anterior tegmental nucleus	AT[e]	n/a	n/a	n/a
Lateral terminal nucleus of accessory optic tract	LT	−	−	−
Midbrain, behavioral state related [MBsta]				
Substantia nigra, compact part	SNc	+	+	−
Pedunculopontine nucleus	PPN	+	+	−
Midbrain raphe nuclei	RAmb	++	+	+
Hindbrain				
Pons				
Pons, sensory related [Psen]				
Nucleus of the lateral lemniscus	NLL	+	+	−
Principal sensory nucleus of the trigeminal	PSV	n/a	+	n/a
Parabrachial nucleus	PB	n/a	++	n/a
Superior olivary complex	SOC	n/a	+	n/a

(Continues)

TABLE 5 | (Continued)

Major brain division[a]	Region[b] Subregion	Density of fiber coverage[c] Case 1	Case 7	Intersect
Pons, motor related [Pmot]				
Barrington's nucleus	B	n/a	++	n/a
Dorsal tegmental nucleus	DTN	n/a	+	n/a
Pontine central gray	PCG	n/a	++	n/a
Pontine gray	PG	+	+	+/−
Pontine reticular nucleus, caudal part	PRNc	n/a	+	n/a
Supragenual nucleus	SG	n/a	−	n/a
Supratrigeminal nucleus	SUT	n/a	+	n/a
Tegmental reticular nucleus	TRN	+	+	+/−
Motor nucleus of trigeminal	V	n/a	+	n/a
Pons, behavioral state related [Psat]				
Superior central nucleus raphe	CS	+	+	−
Locus ceruleus	LC	n/a	+	n/a
Laterodorsal tegmental nucleus	LDT	n/a	+	n/a
Nucleus incertus	NI	n/a	+	n/a
Pontine reticular nucleus	PRNr	+	+	+/−
Nucleus of raphe pontis	RPO	n/a	−	n/a
Subceruleus nucleus	SLC	n/a	−	n/a
Sublaterodorsal nucleus	SLD	n/a	+	n/a
Medulla				
Medulla, sensory related [MYsen][d]		n/a	−	n/a
Medulla, motor related [MYmot]				
Abducens nucleus	VI	n/a	−	n/a
Facial motor nucleus	VII	n/a	−	n/a
Accessory facial motor nucleus	ACVII	n/a	−	n/a
Nucleus ambiguous	AMB[e]	n/a	n/a	n/a
Dorsal motor nucleus of vagus nerve	DMX[e]	n/a	n/a	n/a
Gigantocellular reticular nucleus	GRN	n/a	+	n/a
Infracerebellar nucleus	ICB[e]	n/a	n/a	n/a
Inferior olivary complex	IO[e]	n/a	n/a	n/a
Intermediate reticular nucleus	IRN	n/a	+	n/a
Inferior salivatory nucleus	ISN	n/a	−	n/a
Linear nucleus of the medulla	LIN[e]	n/a	n/a	n/a
Lateral reticular nucleus	LRN[e]	n/a	n/a	n/a
Magnocellular reticular nucleus	MARN	n/a	+	n/a
Medullary reticular nucleus	MDRN[e]	n/a	n/a	n/a
Parvicellular reticular nucleus	PARN	n/a	+	n/a
Parasolitary nucleus	PAS[e]	n/a	n/a	n/a
Paragigantocellular reticular nucleus	PGRN[e]	n/a	n/a	n/a
Perihypoglossal nuclei	PHY[e]	n/a	n/a	n/a
Parapyramidal nucleus	PPY	n/a	+	n/a
Vestibular nuclei	VNC	n/a	+	n/a

(Continues)

TABLE 5 | (Continued)

Major brain division[a]	Region[b] Subregion	Density of fiber coverage[c]		
		Case 1	Case 7	Intersect
Nucleus X	x[e]	n/a	n/a	n/a
Hypoglossal nucleus	XII[e]	n/a	n/a	n/a
Nucleus V	y[e]	n/a	n/a	n/a
Medulla, behavioral state related [MYsat]		n/a	+	n/a
Cerebellum [CB][d]		n/a	−	n/a

[a]Nomenclature and organization of brain regions as determined by the *Allen Mouse Brain Atlas* (Wang et al. 2020a).

[b]Regions and subregions are listed in order of appearance anterioposteriorly.

[c]Brain regions exhibiting high (+++), medium (++), low (+), or very low or no (−) of DsRed-immunoreactive fibers. Representative photomicrographs of these amounts of fiber distributions are shown in Figure 5.

[d]Major brain divisions where DsRed-labeled fibers were absent in all subregions.

[e]Regions not available (n/a) for analysis in our histological preparations.

the accessory bulb (AOB; Table 5), however we were unable to capture the AOB in Case 7.

In the hippocampal formation and retrohippocampal formation, DsRed-labeled fibers were only present in Case 7 posteriorly (L78–91; Figure 8s2–z2 and appeared to terminate within the ventral portion of the cornu ammonis (CA) 1 (Figure 8u2–v2), CA3 (Figure 8t2), and ventral subiculum (SUBv; Figure 8v2–y2). The isocortex lacked DsRed-labeled fibers in both Case 1 and Case 7 (Table 5).

3.5.1.2 | Cortical Subplate (CTXsp).

There were few overlapping fibers along the anteroposterior axis of the cortical subplate, although there were sparse DsRed-labeled fibers within the basomedial (BMA; Figure 8e–v) and basolateral (BLA; Figure 8i–v) amygdalar nuclei in Case 1 and Case 7. There were also discrepancies in the relative abundance of DsRed-labeled fibers between the two cases, as Case 1 displayed more fibers in the anterior BMA and BLA (L59–72; Figure 8h1–o1 and Table 5), while Case 7 displayed more fibers in the posterior BMA and BLA (L67–81; Figure 8l2–u2 and Table 5). No fibers were observed in the remaining regions of the CTXsp, including the claustrum (CLA; Figure 8a–m), endopiriform nucleus (EP; Figure 8a–v), lateral amygdalar nucleus (LA; Figure 8k–s), and posterior amygdalar nucleus (PA; Figure 8r–w).

3.5.2 | Cerebral Nuclei

Overall, we observed low to moderate amounts of DsRed-labeled fibers across the cerebral nuclei though fibers were more abundant in Case 7 than Case 1 (Table 5).

3.5.2.1 | Striatum (STR).

The lateral septal complex (LSX) contained a prominent angular fiber band along the border between the caudal (LSc) and rostral (LSr) lateral septum (Figures 5a and 8b–e). DsRed-labeled fibers in the LSr appeared in punctate clusters and retained terminal-like morphology. The striatum-like amygdalar nucleus (sAMY) contained few DsRed-labeled fibers within the medial (MEA; Figure 8i–r) and central amygdalar nuclei (CEA; Figure 8h–q), but this was not reflected in the intersecting maps (Table 5) due to the sparsity of fibers.

Similarly, ventral regions within the striatum (STRv), like the nucleus accumbens (ACB; Figure 8a–c) contained few DsRed-labeled fibers, but this was also not reflected in the intersecting maps (Table 5). We did not observe any fibers in dorsal regions of the striatum (STRd) that comprised the caudoputamen (CP; Figure 8a–s).

3.5.2.2 | Pallidum (PAL).

Moderate amounts of DsRed-labeled fibers were detected in caudal regions of the pallidum (PALc), particularly ventrally within the posterior bed nucleus of the stria terminalis (BSTp; L56–58; Figures 5b and 8e–g), where the fibers appeared as continuous lines. Likewise, there were moderate amounts of DsRed-labeled fibers in ventral regions of the pallidum (PALv), which were mainly located in the medial portion of the substantia innominata (SI; e.g., Figure 8g) and appeared as continuous lines that extended into the amygdalar complex (e.g., Figure 8j). Within medial regions of the pallidum (PALm), some fibers were observed within the medial septal nucleus (MS; Figure 8a–c) and diagonal band nucleus (NDB; Figure 8a–f). Finally, dorsal regions of the pallidum (PALd), including the globulus pallidus (GP; Figure 8e–o) contained few fibers, but they did not overlap between Case 1 and Case 7 (Table 5).

3.5.3 | Thalamus

Within the diencephalon, the thalamus can be divided into subregions based on their main functional outputs, including the sensory–motor cortex (DORsm)-related thalamus and polymodal association cortex (DORpm)-related thalamus. Overall, DsRed-labeled fibers were more abundant within the DORpm, particularly at midline thalamic regions (e.g., Figure 8h).

3.5.3.1 | Sensory–Motor Cortex-Related Thalamus (DORsm).

The subparafascicular nuclei (SPF; Figure 8p–x) comprised DsRed-labeled fibers that appeared as continuous lines in its magnocellular part (SPFm; Figure 7p–r) and parvicellular part (SPFp; Figure 8s–x). Likewise, the subparafascicular area (SPA) contained notable ascending projections along the dorsoventral axis (Figure 8r). Posteriorly within the DORsm, moderate DsRed-labeled fibers were observed
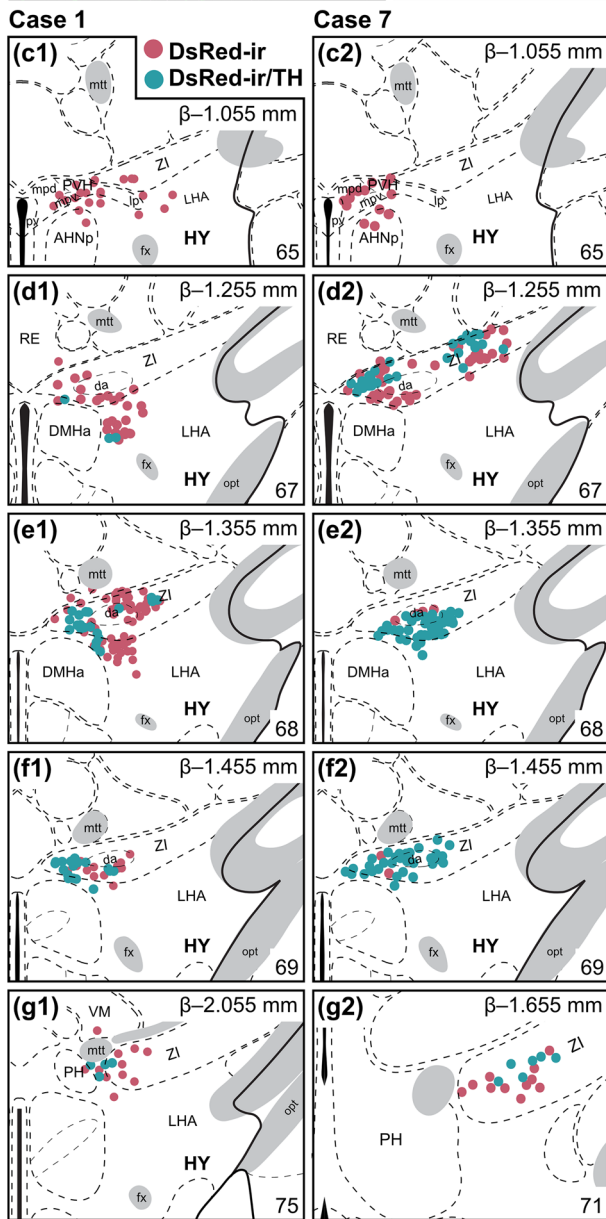
FIGURE 3 | Virally transduced DsRed-immunoreactive enhanced green fluorescent protein (EGFP) cells coexpressed tyrosine hydroxylase (TH) primarily in the medial ZI. Representative photomicrograph of a cre-dependent virus encoding DsRed delivered into the ZI of a *Th-cre;L10-Egfp* mouse (a). High-magnification photomicrograph (from dash outlined area in a) demonstrating EGFP cells (open arrowhead) coexpressing DsRed immunoreactivity (white arrowhead) in the ZI (b). Mapped distribution of DsRed-immunoreactive cells (red circles) coexpressing TH (blue circles) in injection Case 1 (c1–g1) and Case 7 (c2–g2). Cells were mapped onto *Allen Reference Atlas* (*ARA*) templates (Dong 2008) with reference to cytoarchitectural boundaries on Nissl-stained tissue. Panels with maps include the corresponding atlas level (bottom right), bregma (β; top right), and brain region labels using formal nomenclature from the *ARA*. Scale bar: 50 μm (a); 20 μm (b). ZI, zona incerta.

in the peripeduncular nucleus (PP; Figure 8w–y). Within individual injection cases, there were only few fibers forming continuous lines in the ventral group of the dorsal thalamus (VENT; Table 5) that includes the ventral medial nucleus (VM; Figure 8j–r), ventral anterior–lateral complex (VAL; Figure 8i–p), and ventral posterior complex (VP; Figure 8k–t) of the thalamus. Sparse DsRed-labeled fibers were in the geniculate group of the dorsal thalamus (GENd), including the medial geniculate complex (MGd; Figure 8w–y), and the dorsal part of the lateral geniculate complex (LGd; Figure 8p–v).

3.5.3.2 | Polymodal Association Cortex-Related Thalamus (DORpm). Regions along the midline of DORpm, such as the midline group (MTN), medial group (MED), and intralaminar nuclei (ILM) of the dorsal thalamus contained abundant DsRed-labeled fibers. The MTN closely neighbors the ZI, and regions like the nucleus of reuniens (RE; Figure 8f–q) and paraventricular nucleus of the thalamus (PVT; Figures 5c and 8e–r) were heavily labeled with DsRed fibers displaying a clustered morphology. For instance, the RE contained dense axon terminals that skirted the parataenial nucleus to innervate the anterior PVT (Figures 5d and 8g–i). Likewise, nuclei in the MED, such as the intermediodorsal nucleus of the thalamus (IMD; Figure 8k–r), which lies between the PVT and RE, also contained dense DsRed-labeled fibers, but they appeared as continuous lines (e.g., Figure 8n). Consistently, medial structures within the intralaminar nuclei of the thalamus (ILM), including the central medial (CM; Figure 8h–q) and central lateral (CL; Figure 8k–q) nucleus of the thalamus, contained moderate DsRed-labeled fibers forming continuous lines. Although located laterally, the geniculate group of the ventral thalamus (GENv) also contained moderate DsRed-labeled fibers with continuous line morphology, particularly within the intergeniculate leaflet of the lateral geniculate complex (IGL; Figure 8s–v).

Few DsRed-labeled fibers were observed within the lateral (LAT) and anteroventral (ATN) groups of the dorsal thalamus as well as the epithalamus. Notably, within the LAT, the lateral posterior nucleus of the thalamus (LP; Figure 8n–w) contained the most DsRed-labeled fibers, particularly within the dorsomedial portion (e.g., Figure 8r). The remaining LAT regions such as the posterior complex of the thalamus (PO; Figure 8l–u) contained few DsRed-labeled fibers. Majority of the anterior thalamic regions, including the anteroventral (AV; Figure 8g–k) and anterodorsal (AD; Figure 8g–j) nucleus of the thalamus, had sparse DsRed-labeled fibers. Lateral to the AD and AV, DsRed-labeled fibers strikingly surrounded the lateral (Figure 8i,j) and dorsal border (Figure 8k–n) of the lateral dorsal nucleus of the thalamus (LD). In the epithalamus, comprising the medial (MH; Figure 8j–s) and lateral habenula (LH; Figure 8k–s), DsRed fibers were sparse, despite the abundance of DsRed fibers in neighboring regions like PVT and CM. Similarly, we seldom observed DsRed-labeled fibers in the reticular thalamus (RT; Figure 8h–r), despite the RT being in close proximity to the ZI.
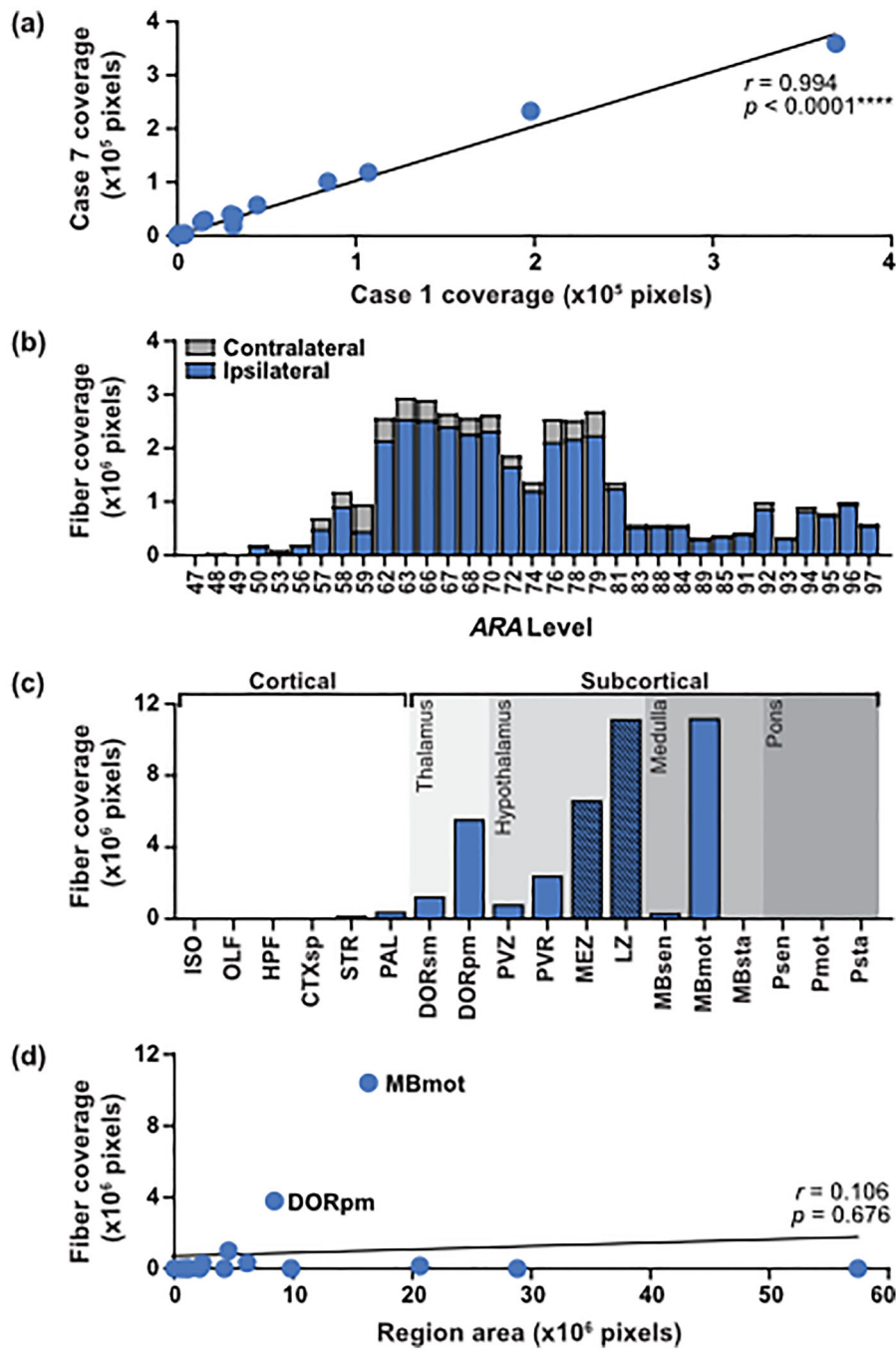
FIGURE 4 | Motor-related midbrain comprised the most abundant fiber projections from *Th-cre* zona incerta (ZI) cells. Correlation of fiber coverage (in pixels) between injection Case 1 and Case 7 across major brain divisions (see Supporting Information Figure 1) as defined by the Allen Mouse Brain Atlas (Wang et al. 2020a; Allen Institute for Brain Science 2011; a). The amount of contralateral and ipsilateral fiber coverage formed by intersecting points between Case 1 and Case 7 throughout the entire brain (b). Amount of fiber coverage from intersecting points across each major division of the brain (c) with hatched bars indicating regions comprising the injection site. Correlation of fiber coverage from intersecting points and total region area (in pixels; d). Correlational analyses were determined by Pearson's *r*, where ****, $p < 0.0001$. CTXsp, cortical subplate; DORpm, polymodal-association cortex-related regions of the thalamus; DORsm, sensory–motor cortex-related regions of the thalamus; HPF, hippocampal formation; ISO, isocortex; LZ, hypothalamic lateral zone; MBmot, motor-related regions of the midbrain; MBsen, sensory-related regions of the midbrain; MBsta, behavior-state-related regions of the midbrain; MEZ, hypothalamic medial zone; OLF, olfactory regions of the cortex; PAL, pallidum; Pmot, motor-related regions of the pons; Psen, sensory-related regions of the pons; Psta, behavior-state-related regions of the pons; PVR, periventricular region; PVZ, periventricular zone; STR, striatum.
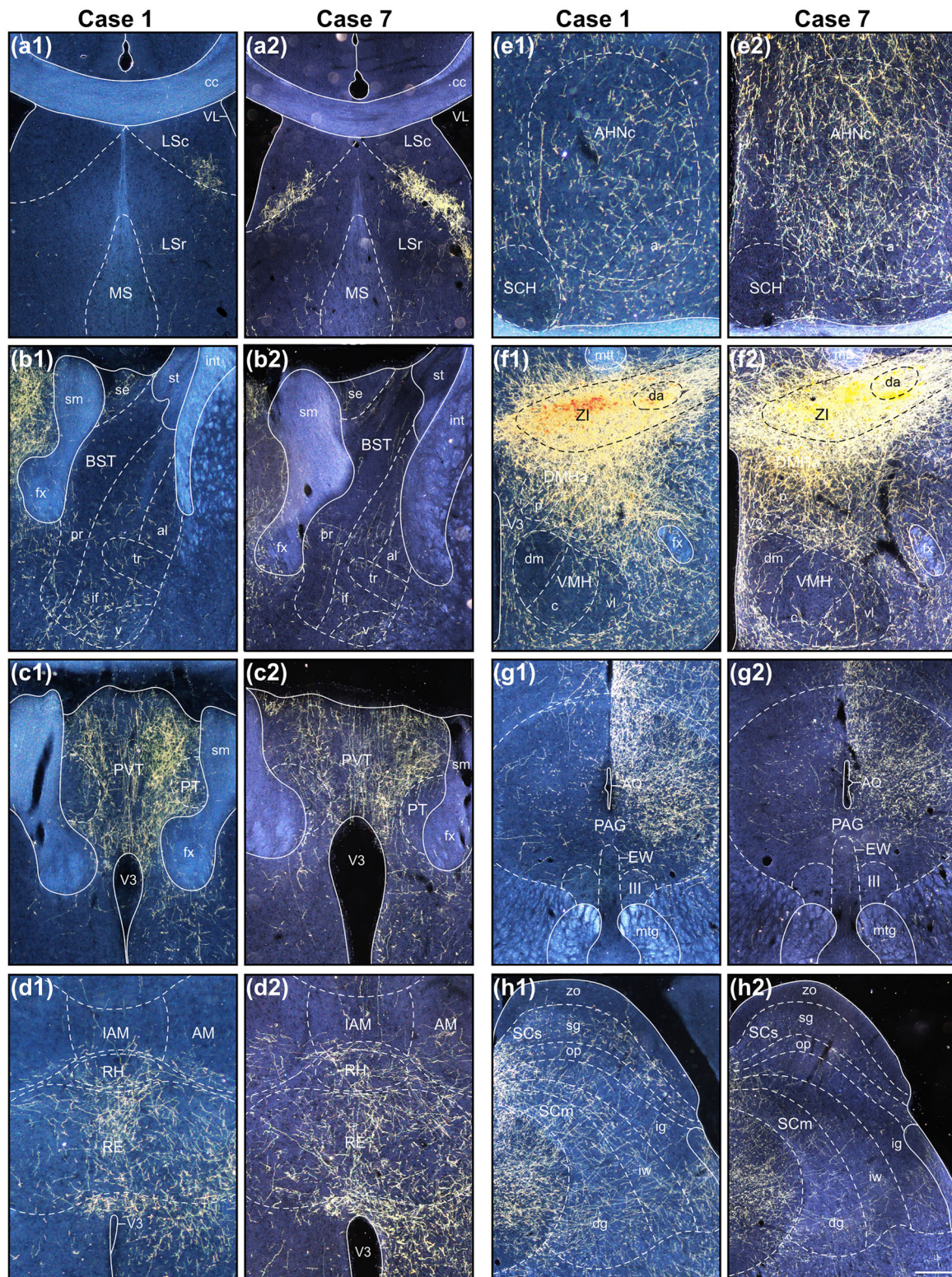
FIGURE 5 | DsRed-labeled fibers from *Th-cre* ZI cells are abundant throughout the brain. Representative darkfield photomicrographs of DsRed-immunoreactive fibers from injection Case 1 (a1–h1) and Case 7 (a2–h2). Scale bar, 50 µm. AHN, anterior hypothalamic nucleus; AHNa, anterior part; AHNc, central part; AM, anteromedial nucleus of the thalamus; AQ, cerebral aqueduct; BST, bed nucleus of the stria terminalis; BSTal, BST anterolateral area; BSTif, BST interfascicular nucleus; BSTpr, BST principle nucleus; BSTse, BST strial extension; BSTv, ventral nucleus; cc, corpus callosum; DMH, dorsomedial hypothalamic nucleus; DMHa, DMH anterior part; DMHp, DMH posterior part; EW, Edinger–Westphal nucleus; fx, fornix; IAM, interanteromedial nucleus of the thalamus; III, oculomotor nucleus; int, internal capsule; LS, lateral septal nucleus; LSc, LS caudal (caudodorsal) part; LSr, LS rostral (rostroventral) part; MS, medial septal nucleus; mtg, mammillotegmental tract; mtt, mammillothalamic tract; PAG, periaqueductal gray area; PT, paratenial nucleus; PVT, paraventricular nucleus of the thalamus; RE, nucleus of reuniens; RH, rhomboid nucleus; SCH, suprachiasmatic nucleus; SCm, superior colliculus, motor related; SCdg, SCm deep gray layer; SCig, SCm intermediate gray layer; SCiw, SCm intermediate white layer;

SCs, superior colliculus, sensory related; SCop, SCs optic layer; SCsg, SCs superficial gray layer; SCzo, SCs zonal layer; sm, stria medullaris; st, stria terminalis; tr, transverse nucleus; V3, third ventricle; VL, lateral ventricle; VMH, ventromedial hypothalamic nucleus; VMHc, central part; VMHdm, dorsomedial part; VMHvl, ventrolateral part; ZI, zona incerta; ZIda, dopaminergic A13 group.
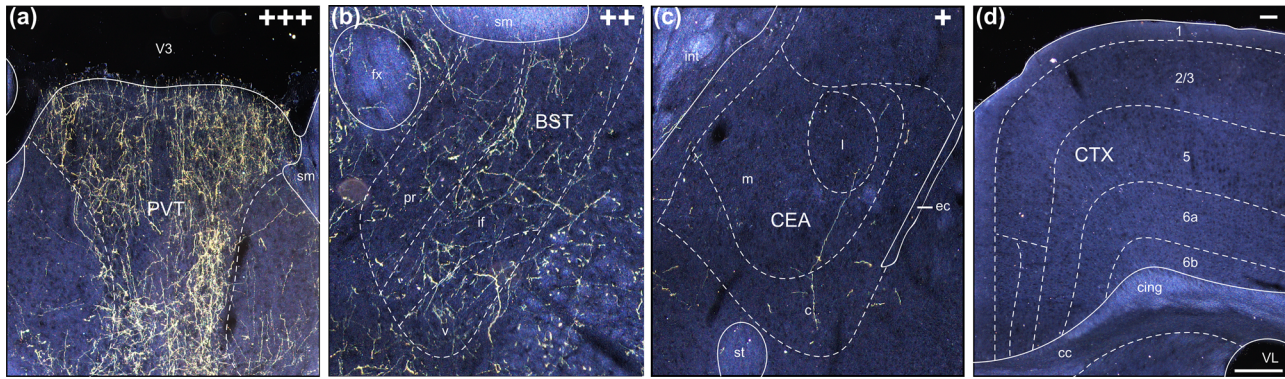

FIGURE 6 | Difference in density of DsRed-labeled fibers from *Th-cre* zona incerta (ZI) cells. Representative darkfield photomicrographs of DsRed-immunoreactive fibers providing high (+++; a), moderate (++; b), low (+; c), and very little or no fiber coverage (−; d) following cre-mediated viral transduction of *Th-cre* cells in the medial ZI. Scale bar, 50 μm. 1, layer 1; 2/3, layer 2/3; 5, layer 5; 6a, layer 6a; 6b, layer 6b; sm, stria medullaris; st, stria terminalis; BST, bed nucleus of the stria terminalis; BSTif, BST interfascicular nucleus; BSTpr, BST principle nucleus; BSTv, BST ventral nucleus; cc, corpus callosum; CEA, central amygdala; CEAl, CEA lateral part; CEAm, CEA medial part; CEAc, CEA central part; cing, cingulum bundle; CTX, cortex; ec, external capsule; fx, fornix; int, internal capsule; PVT, paraventricular nucleus of the thalamus; V3, third ventricle; VL, lateral ventricle.

3.5.4 | Hypothalamus

The diencephalon also includes the hypothalamus, which comprised DsRed-labeled fibers throughout its rostrocaudal extent (Table 5).

3.5.4.1 | Periventricular Zone (PVZ). The paraventricular hypothalamic nucleus (PVH) contained abundant DsRed-labeled fibers, particularly within the parvicellular (PVHp; Figure 8e–k) and magnocellular divisions (PVHm; Figure 8i,j). Among regions abutting the third ventricle, DsRed-labeled fibers were observed in the anterior (PVa; Figure 8h) and intermediate part (PVi; Figure 8i–k) of the periventricular hypothalamic nucleus. However, the arcuate hypothalamic nucleus (ARH; Figure 8k–q) contained moderate amounts of DsRed-labeled fibers that appeared in clusters, particularly at anterior levels (L66–67; Figure 8k,l). DsRed-labeled fibers with clustering morphology were present in the supraoptic nucleus (SO) of Case 7 (Figure 8e2–j2) but largely avoided the SO in Case 1 (Figure 8e1–j1).

3.5.4.2 | Periventricular Region (PVR). Dense clustering fibers were observed in the neighboring subparaventricular zone (SBPV; Figure 8i,j) and posteriorly in the dorsomedial hypothalamic nucleus (DMH; Figure 8l–q), which was more prominent in Case 7 (Figure 8l2–q2). Anteriorly, the median preoptic nucleus (MEPO; Figure 8b–d) and medial preoptic area (MPO; Figure 8b–g) contained a low to moderate density of widely distributed DsRed-labeled fibers displaying clustering morphology.

Sparse DsRed-labeled fibers were observed in the ventrolateral (VLPO; Figure 8d), anterodorsal (ADP; Figure 8c,d), and anteroventral preoptic nucleus (AVP; Figure 8c,d), anteroventral periventricular nucleus (AVPV; Figure 8c,d), and suprachiasmatic nucleus (SCH; Figure 8f–i). Although individual injection cases displayed moderate densities of DsRed-labeled fibers, the intersecting maps revealed minimal fibers in the posterior part (PVp; Figure 8r–t) and preoptic part (PVpo; Figure 8e–g) of the PV. Individual injection cases contained sparse DsRed-labeled fibers in the parastrial nucleus (PS; Figure 8d), although this was not reflected in the intersecting maps. We found no DsRed-labeled fibers in the vascular organ of the lamina terminalis (OV; Figure 8b,c) and subfornical organ (SFO; Figure 8g–i). Unfortunately, we were unable to capture the posterodorsal preoptic nucleus (PD), as we did not collect the level containing this region.

3.5.4.3 | Medial Zone (MEZ). DsRed-labeled fibers that appeared as clusters were abundant within regions near the injection site (Figure 5f), including the anterior hypothalamic nucleus (AHN; Figure 5e and 8g–k) and descending division of the PVH (PVHd; Figure 8i,j). In posterior regions, abundant DsRed-labeled fibers were within the posterior hypothalamus (PH), which contained fibers that formed clusters or continuous lines that traveled toward the PAG (e.g., Figure 8s–u).

Interestingly, DsRed-labeled fibers largely avoided the ventromedial hypothalamic nucleus (VMH; Figure 8k–o) though a few axons may pass through the VMH at posterior levels (L70–73; Figure 8n–p). Light to moderate DsRed-labeled fibers were observed in the ventral (PMv) and dorsal (PMv) premammillary nuclei (Figure 8r,s) with even fewer fibers found at the ventrolateral border of the mammillary body (MBO; Figure 8r–w) and medial preoptic nucleus (MPN).

3.5.4.4 | Lateral Zone (LZ). The injection site largely encompassed the LZ, so it was difficult to differentiate fibers-of-passage from terminal sites of DsRed-labeled fibers. DsRed-labeled fibers in the ZI (Figure 5f1 and 8i–v) were
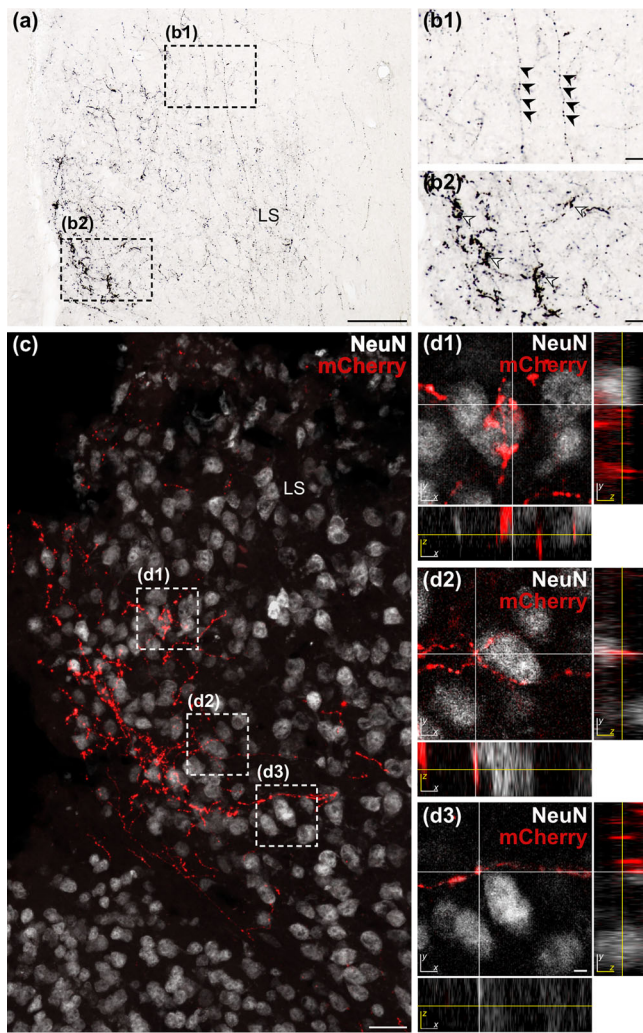
FIGURE 7 | *Th-cre* zona incerta (ZI) fibers appear as continuous lines or clusters at target sites. Representative brightfield photomicrographs of DsRed-immunoreactive fibers from Cre-mediated *Th-cre* ZI cells (a) revealing fibers that were arranged in a continuous line (black arrowheads; b1) or that formed clusters (white arrowheads; b2). Representative confocal photomicrographs of mCherry-immunoreactive fibers (c) with orthogonal projections from the *xz* or *yz* plane showing no discernible space at appositions between cluster-like mCherry-labeled fibers and NeuN-immunoreactive cell bodies (d1) and mCherry-labeled fibers appearing as continuous lines that directly contact (d2) or avoid (d3) NeuN-labeled cells. Scale bars: 50 µm (a); 20 µm (b); 50 µm (c); *x, y, z* axis: 5 µm (d). LS, lateral septum.

abundant and appeared to travel laterally and arrive at the anterior and caudal parts of the thalamus and midbrain.

DsRed-labeled fibers in the lateral hypothalamic area (LHA) varied across *ARA* levels. Majority of DsRed-labeled fibers in the LHA at L67–76 were concentrated dorsal to the fornix (Figure 8l–r). The anterior LHA (L62–66; Figure 8i–k) contained relatively sparse axons. In contrast, more anterior regions like the lateral preoptic area (LPO; Figure 7a–g), retrochiasmatic area (RCH; Figure 8i,j) contained moderate fibers. Posteriorly, there were also moderate fibers within the tuberal nucleus (TU; Figure 8k–q), parasubthalamic (PSTN; Figure 8p–s). Few fibers were within the

preparasubthalamic (PST; Figure 8o) and subthalamic nucleus (STN; Figure 8o–s).

3.5.4.5 | Median Eminence. DsRed-labeled fibers were detected in the median eminence (ME) of Case 7 (Figure 8n2–q2) but not Case 1 (Figure 8n1–q1). It was unclear whether DsRed-labeled fibers in the ME targeted the internal or external lamina in our tissue.

3.5.5 | Midbrain

The midbrain spans L77–113 and can be further subdivided as sensory related (MBsen), motor related (MBmot), or behavior-state related (MBsta). Unfortunately, we were only able to collect brain sections up to *ARA* L97 for Case 1, thus descriptions of DsRed-labeled fibers posterior to L97 are from Case 7 only. Overall, DsRed-labeled fibers were most abundant within the MBmot (Table 5).

3.5.5.1 | Sensory-Related Midbrain (MBsen). The MBsen largely comprises the dorsal aspect of the superior colliculus (SC) and inferior colliculus (IC). DsRed-labeled fibers were relatively low within the dorsal SC including the optic (SCop), superficial gray (SCsg), and zonal layer (SCzo), and most fibers, which formed continuous lines, were medially distributed within the SCsg (Figures 5h, 8w–ff, and 9a,b). The entire IC belongs to the sensory-related part of the midbrain and had moderate but prominent DsRed-labeled fibers in the external nucleus (ICe) and dorsal nucleus (ICd) anteriorly (e.g., Figure 9b–e). However, there were DsRed-labeled fibers also in the central nucleus (ICc) posteriorly (Figure 9f). Abundant DsRed-labeled fibers were also observed in nuclei within the PAG area such as the medial trigeminal nucleus (MEV; Figure 9a–c).

There were also low amounts of DsRed-labeled fibers in a collection of brain regions located ventral to the SC and IC that included the nucleus of the brachium (NB; Figure 8aa), nucleus sagulum (SAG; Figure 8ee,ff), and parabigeminal nucleus (PBG; Figure 8cc–ff).

3.5.5.2 | Motor-Related Midbrain (MBmot). In the dorsal part of the brain, DsRed-labeled fibers were densest and abundant throughout the anteroposterior extent in the PAG and the motor-related SC, but the fiber distribution varied spatially within these regions. Specifically, DsRed-labeled fibers appearing as clusters concentrated in the dorsal region of the PAG (Figure 5g; e.g., Figure 8z3–ff3) and along the medial column of the ventral aspects of the SC, especially the deep gray layer (SCdg) and intermediate white layer (SCiw; Figures 5h, 8v–ff, and 9a,b). Ventral to the PAG, midline structures like the oculomotor nucleus (III; e.g., Figure 8bb), trochlear nucleus (IV; Figure 8ff), red nucleus (RN; e.g., Figure 8cc), Edinger–Westphal nucleus (EW; Figure 8y,z), and ventral tegmental nucleus (VTN; Figure 9a,b) were devoid of DsRed-labeled fibers. Lateral to the PAG, the cuneiform nucleus (CUN) comprised moderate fibers anteriorly (Figure 9a–d), while the lateral terminal nucleus of the accessory optic tract (LT; Figure 9u,v) was devoid of fibers.

In the ventral part of the brain, DsRed-labeled fibers in the midbrain reticular nucleus (MRN; Figures 8t–ff and 9a,b), includ-
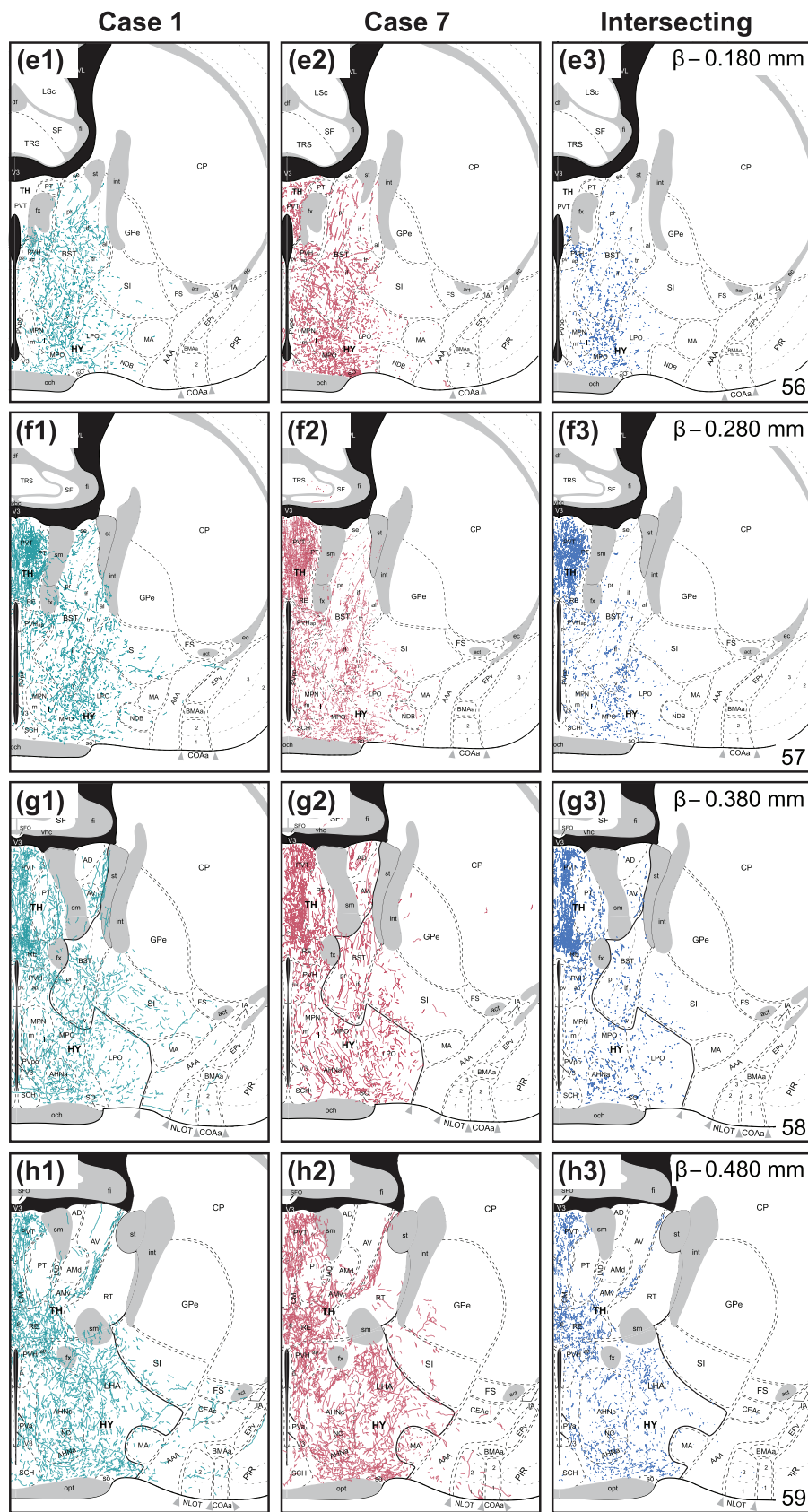
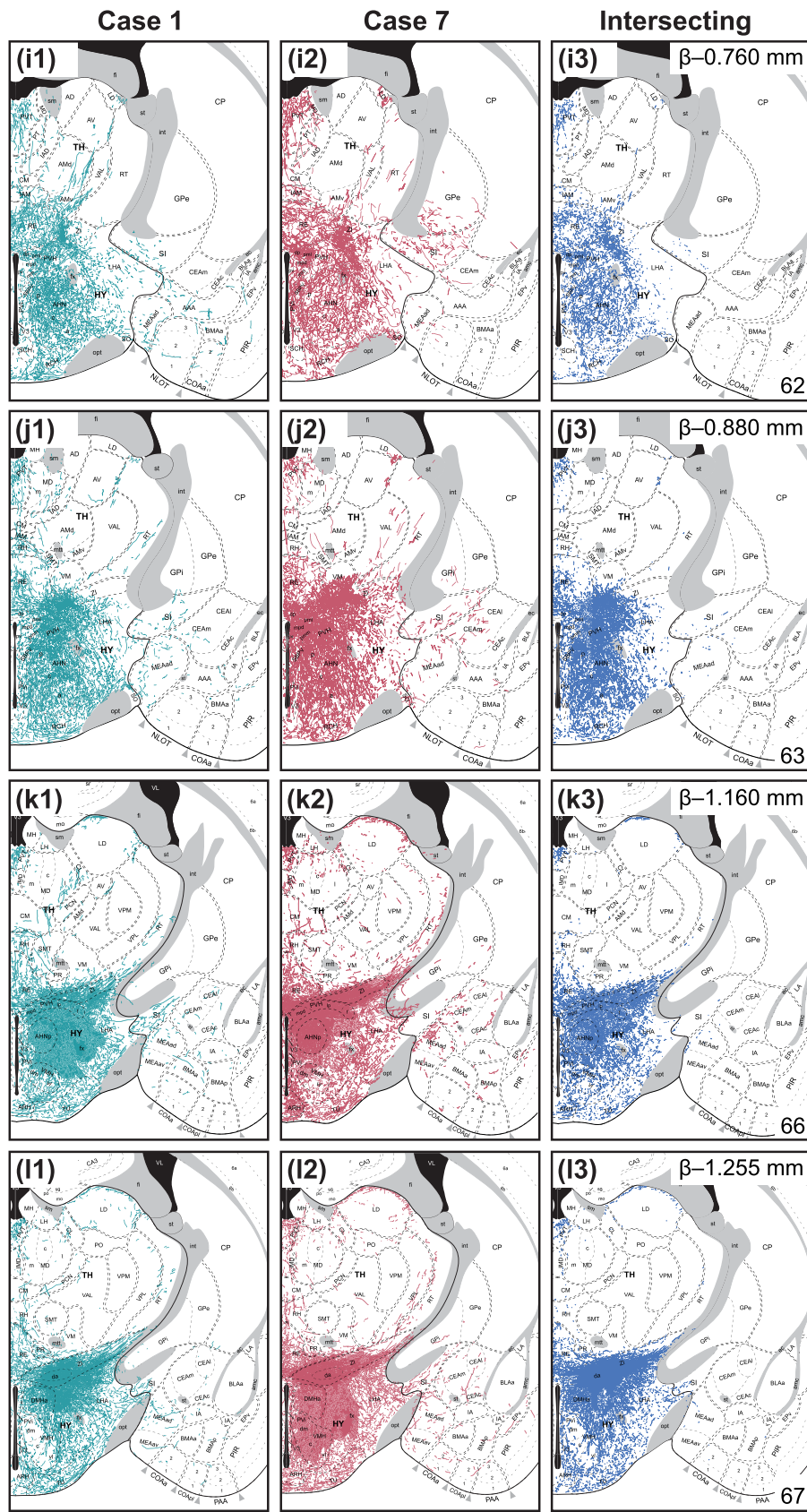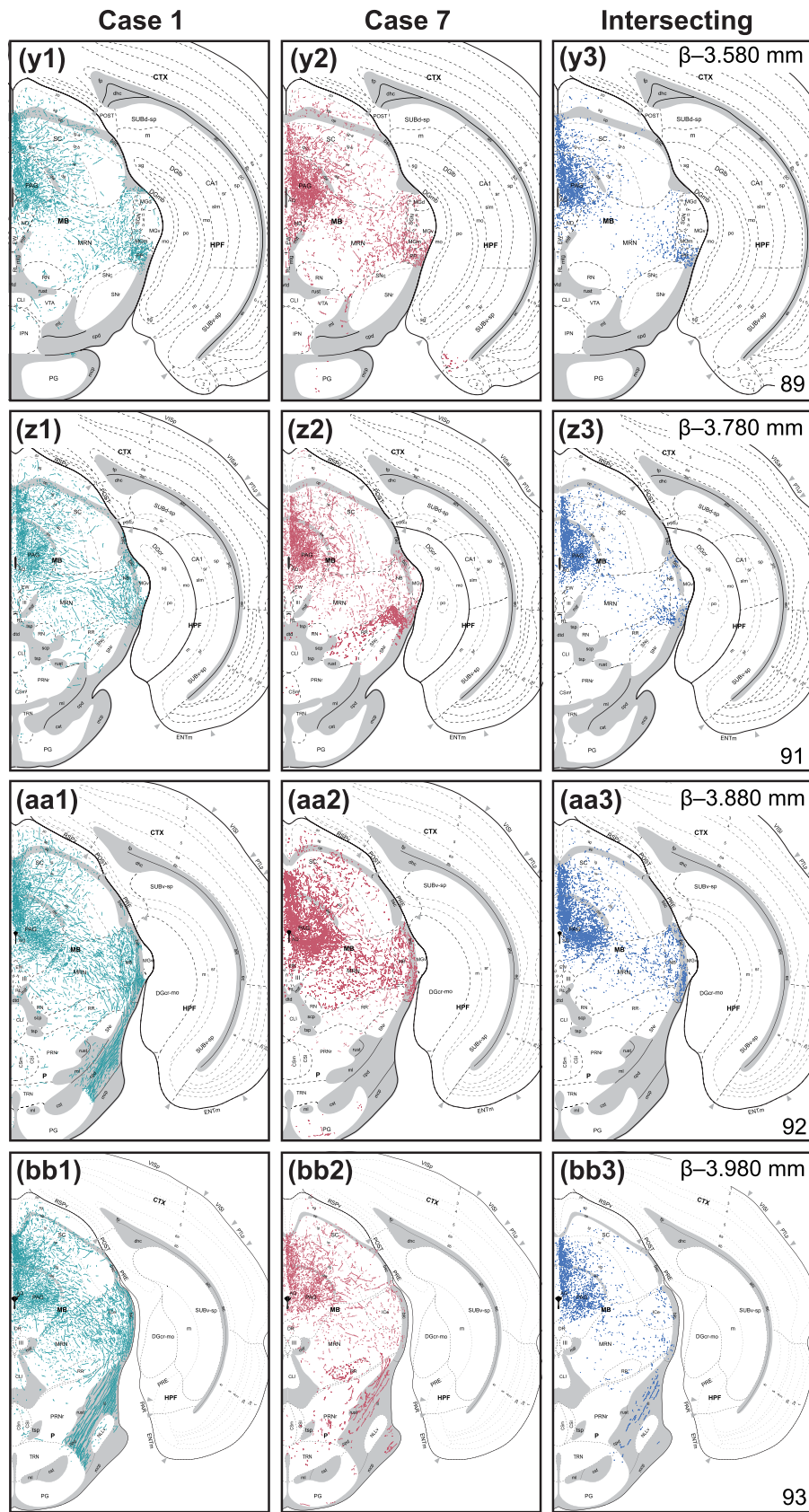**FIGURE 8** | Distribution of fiber projections from *Th-cre* zona incerta (ZI) cells from the forebrain to midbrain. Mapped distribution of fibers from injection Case 1 (a1–ff1), Case 7 (a2–ff2), and the points of intersection between both injection cases (a3–ff3). Traced fibers were overlaid onto *Allen Reference Atlas* (*ARA*) templates (Dong 2008) with reference to cytoarchitectural boundaries on Nissl-stained tissue. Panels include the corresponding atlas level (bottom right), bregma (β; top right), and brain region labels using formal nomenclature from the *ARA*.

Case 1	Case 7	Intersecting
(e1)	(e2)	(e3) β − 0.180 mm
(f1)	(f2)	(f3) β − 0.280 mm
(g1)	(g2)	(g3) β − 0.380 mm
(h1)	(h2)	(h3) β − 0.480 mm

FIGURE 8 | (Continued)

Case 1	Case 7	Intersecting

FIGURE 8 | (Continued)

Case 1 | **Case 7** | **Intersecting**

(m1) ... (m2) ... (m3) β−1.355 mm ... 68

(n1) ... (n2) ... (n3) β−1.550 mm ... 70

(o1) ... (o2) ... (o3) β−1.760 mm ... 72

(p1) ... (p2) ... (p3) β−1.855 mm ... 73

FIGURE 8 | (Continued)

Case 1 | **Case 7** | **Intersecting**

(q1) | (q2) | (q3) β–1.955 mm | 74
(r1) | (r2) | (r3) β–2.155 mm | 76
(s1) | (s2) | (s3) β–2.355 mm | 78
(t1) | (t2) | (t3) β–2.480 mm | 79

FIGURE 8 | (Continued)

FIGURE 8 | (Continued)

Case 1	Case 7	Intersecting

FIGURE 8 | (Continued)

	Case 1	Case 7	Intersecting
	(cc1)	(cc2)	(cc3) β–4.080 mm
	(dd1)	(dd2)	(dd3) β–4.155 mm
	(ee1)	(ee2)	(ee3) β–4.280 mm
	(ff1)	(ff2)	(ff3) β–4.380 mm
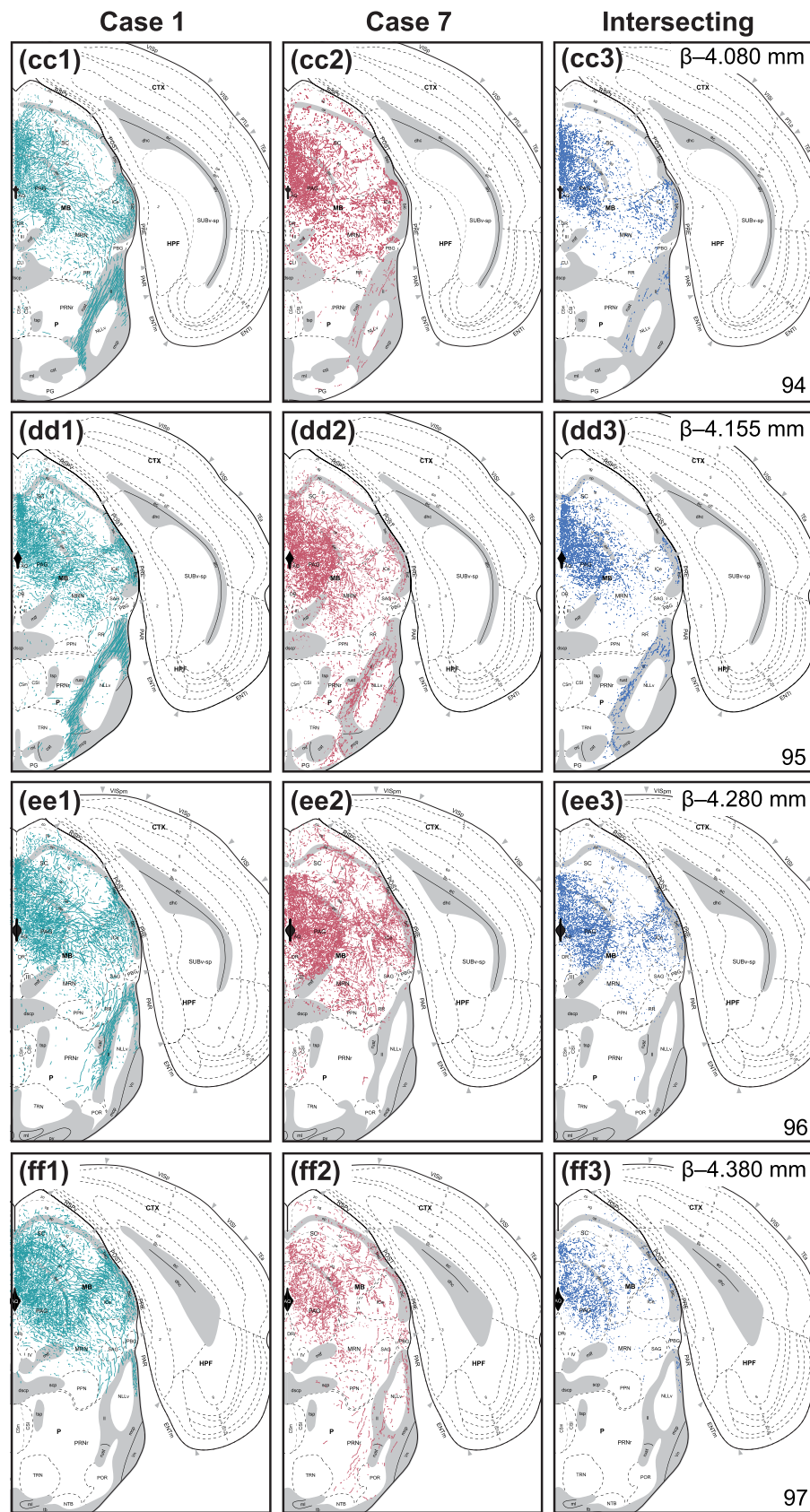
FIGURE 8 | (Continued)
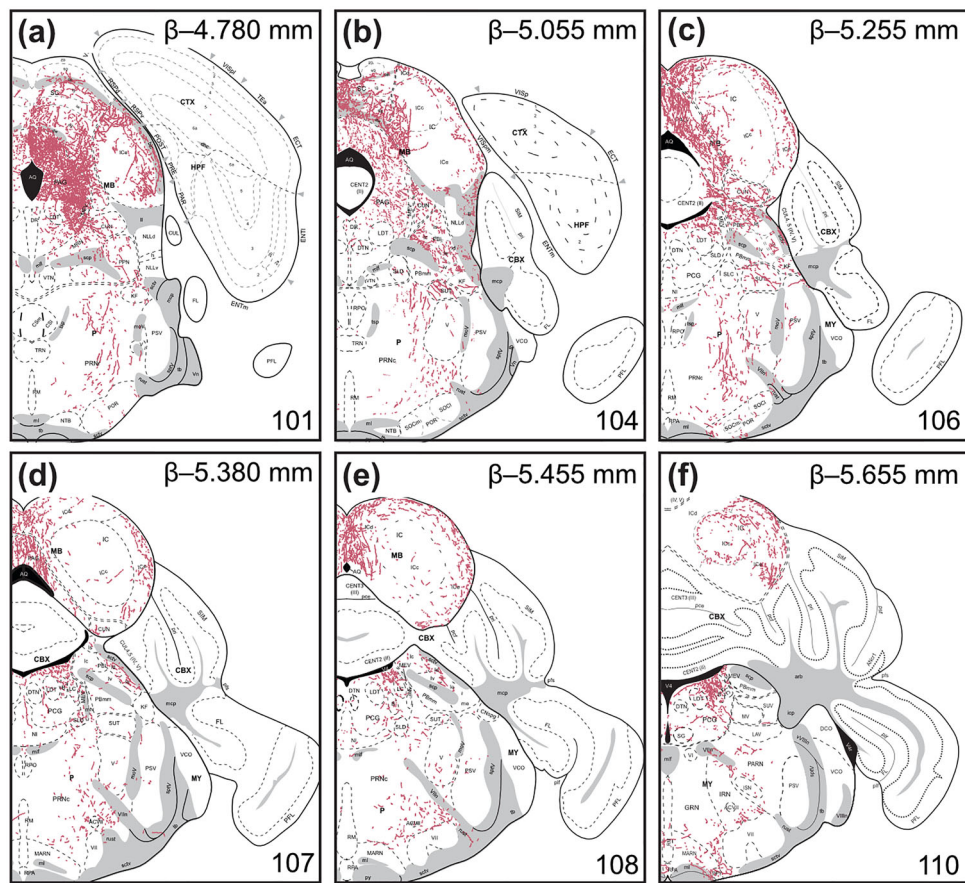
FIGURE 9 | Distribution of fiber projections from *Th-cre* zona incerta (ZI) cells in the hindbrain. Mapped distribution of fibers from injection Case 7 with reference to cytoarchitectural boundaries from Nissl-stained tissue using *Allen Reference Atlas* (*ARA*) templates (Dong 2008; a–f). Panels include the corresponding atlas level (bottom right), bregma (β; top right), and brain region labels using formal nomenclature from the *ARA*.

ing its retrorubral area (RR; Figure 8z–ee), were moderate and distributed laterally as fibers that formed continuous lines. Fibers in the VTA (Figure 8t–z) were more prominent in the anterior (L81–83; Figure 8u,v) than posterior levels (L84–91; Figure 8w–z). However, there were no fibers in the reticular part of the substantia nigra (SNr; Figure 8t–aa).

In the pretectal region, DsRed-labeled fibers were especially prevalent medially, for example, in the medial pretectal area (MPT; Figure 8s–u) and less so in the nucleus of the posterior commissure (NPC; Figure 8s–u), olivary pretectal nucleus (OP; Figure 8s–u), and posterior pretectal nucleus (PPT; Figure 8u). Other divisions of the pretectal region like the anterior pretectal region (APN; Figure 8s–w) and nucleus of the optic tract (NOT; Figure 8u–w) were sparsely innervated. Unfortunately, we were unable to capture the anterior tegmental nucleus (AT) as it fell between levels that we did not collect for either injection case.

3.5.5.3 | Behavioral State-Related Midbrain (MBsta).

There were few, if any, DsRed-labeled fibers in the compact part of the substantia nigra (SNc; Figure 8u–z), pedunculopontine nucleus (PPN; Figures 8dd–ff and 9a), or midbrain raphe nuclei (RAmb; Figures 8v–ff and 9a,b).

3.5.6 | Pons

Overall, DsRed-labeled fibers were sparse throughout the pons (Table 5).

3.5.6.1 | Sensory-Related Pons (Psen).

There were moderate fibers in the lateral division of the parabrachial nucleus (PBl; Figure 9b–e) but fewer in the medial division (PBm; Figure 9b–f). Few DsRed-labeled fibers were present in the nucleus of the lateral leminscus (NLLv; Figures 8bb–ff and 9a,b), principal sensory nucleus of the trigeminal (PSV; Figure 9a–f), and superior olivary complex (SOC; Figures 8ee,ff and 9a–c). There were no fibers in the Kölliker–Fuse subnucleus (KF; Figure 9a–d).

3.5.6.2 | Motor-Related Pons (Pmot).

There were moderate amounts of DsRed-labeled fibers displaying a clustering morphology in the pontine central gray (PCG; Figure 9c–f) toward the dorsolateral aspect of the region. With the exception of Barrington's nucleus (B; Figure 9d–f), which contained considerable fibers, PCG nuclei such as the dorsal tegmental nucleus (DTN; Figure 9b–f) and supragenual nucleus (SG; Figure 9f) contained little to no fibers.

There were only few fibers forming continuous lines anteriorly in the pontine gray (PG; Figure 8x–dd), tegmental reticular nucleus (TRN; Figures 8z–ff and 9a,b), and supratrigeminal nucleus (SUT;

Figure 9b–e). There were more fibers laterally in the caudal part of the pontine reticular nucleus (PRNc; Figure 9b–e), but they largely avoided the motor nucleus of trigeminal (V; Figure 9a–e).

3.5.6.3 | Behavioral-State-Related Pons (Psta). This brain division contained very few DsRed-labeled fibers overall. Medial structures like the superior central nucleus raphe (CS; Figures 8z–ff and 9a), nucleus incertus (NI; Figure 9c–e), and nucleus raphe pontis (RPO; Figure 9b–d) were particularly devoid of fibers. Laterally, the locus ceruleus (LC; Figure 9d–f) and rostral part of the PRN (PRNr; Figures 8z–ff and 9a) contained a few fibers. Interestingly, while the PAG contained abundant DsRed-labeled fibers, nuclei within the PAG such as the laterodorsal nucleus (LDT; Figure 9b–f) did not contain fibers, while the sublaterodorsal nucleus (SLD; Figure 9b–e) contained very few. Ventral to the PAG, the subceruleus nucleus (SLC; Figure 9b,c) was also devoid of fibers.

3.5.7 | Medulla

The medulla spans the remainder of the hindbrain (L97–L132), but our analyses only extended until L110. Most DsRed-labeled fibers within the medulla were distributed ventrolaterally and within motor-related regions of the medulla (MYmot; Table 5).

3.5.7.1 | Sensory-Related Medulla (MYsen). No DsRed-labeled fibers were found within MYsen (Figures 8ff and 9a–f). DsRed-labeled fibers appeared in neighboring ventral regions like the PRNc in the pons but avoided MYsen regions like the nucleus of the trapezoid body (NTB; Figures 8ff and 9a,b).

3.5.7.2 | Motor-Related Medulla (MYmot). Majority of fibers are observed within the gigantocellular (GRN), intermediate (IRN), and magnocellular (MARN) reticular nucleus (MARN; Figure 9f). Fibers within these regions appeared in the ventrolateral direction and hug the border of the facial motor nucleus (VII), which was devoid of fibers (e.g., Figure 9f). A few DsRed-labeled fibers were also seen in the parvicellular reticular thalamus (PARN; Figure 9f). Reticular thalamic nuclei such as the gigantocellular (GRN; Figure 9f) and intermediate reticular nucleus (IRN; Figure 9f) also contained fibers, but these were sparse and appeared as continuous lines.

Sparse DsRed-labeled fibers forming continuous lines were observed in the parapyramidal nucleus (PPY; Figure 9f) and vestibular nuclei (VNC; Figure 9f). No fibers were observed in the abducens nucleus (VI; Figure 9f), accessory facial motor nucleus (ACVII; Figure 9d–f), and inferior salivary nucleus (ISN; Figure 9f). Unfortunately, we were unable to collect posterior sections comprising the nucleus ambiguus (AMB), dorsal motor nucleus of the vagus nerve (DMX), infracerebellar nucleus (ICB), inferior olivary complex (IO), linear nucleus of the medulla (LIN), lateral reticular nucleus (LRN), parasolitary nucleus (PAS), perihypoglossal nuclei (PHY), nucleus x (x), hypoglossal nucleus (XII), or nucleus y (y).

3.5.7.3 | Behavioral-State-Related Medulla (MYsta). None of the midline nuclei, including the nucleus raphe magnus (RM; Figures 8ff and 9a–f) or nucleus raphe pallidus (RPA; Figure 9c–f) in this subdivision contained DsRed-labeled fibers.

3.5.8 | Cerebellum

We were unable to capture the entire rostrocaudal extent of the cerebellum from Case 1 or Case 7, but we did not observe DsRed-labeled fibers in the cerebellum in the sections we collected (up to L110; Figure 9b–f). However, we were able to confirm the lack of DsRed-labeled fibers in the caudal cerebellum using tissue from other injection cases (e.g., Cases 2–6).

4 | Discussion

The ZI is a narrow GABAergic region in the hypothalamus that extends mediolaterally and rostrocaudally through the hypothalamus. One subpopulation of GABAergic ZI cells also produce DA, and these $ZI^{DA/GABA}$ cells are marked by TH immunoreactivity (Negishi et al. 2020). Interestingly, $ZI^{DA/GABA}$ cells are found only within a narrow 300-µm range of the rostral ZI and do not colocalize with neuropeptides like melanin-concentrating hormone in the ZI (Negishi et al. 2020; Miller et al. 2024), chemical messengers like glutamate (Negishi et al. 2020), or other catecholamines like noradrenaline or adrenaline (Negishi et al. 2020). However, GABAergic ZI cells may be defined by additional markers like somatostatin (Kolmac and Mitrofanis 1999) and calretinin (Li et al. 2021), but medial TH-ir $ZI^{DA/GABA}$ cells did not display either somatostatin or calretinin immunoreactivities. Other calcium-binding proteins like calbindin (Li et al. 2021) or parvalbumin (Kolmac and Mitrofanis 1999) have also been reported in the ZI but are known to be caudally distributed in the ZI (Watson et al. 2014) and were thus not expected to colocalize with TH ZI cells. Together, these findings suggested that TH-expressing $ZI^{DA/GABA}$ cells form a distinct subpopulation of medial ZI cells. We determined the projection targets of TH cells from the medial ZI by tracing and mapping the distribution of fibers throughout the brain of *Th-cre* cells. Almost all ZI *Th-cre* cells expressed *Th* mRNA, but only medially distributed ZI *Th-cre* cells coexpressed TH immunoreactivity, hence we expected that only medial ZI *Th-cre* cells would produce DA.

We selected two injection cases that differed in TH coexpression at ZI *Th-cre* cells to trace and map their brainwide projections and assess differences between their fiber distribution. Interestingly, we did not observe stark differences in the brain regions labeled, which suggested that TH protein expression minimally affected the distribution of axonal projections from *Th-cre* cells. Given their similarities in projections, we overlapped the mapped fibers from both cases to identify their intersecting points and delineated spatial regions comprising fibers from GABAergic ZI DA cells. We found that DsRed-labeled fibers were distributed throughout the brain but were most prominent in the PAG at MBmot and paraventricular thalamic (PVT) nucleus at DORpm.

The ZI has been further subdivided into rostral or caudal and dorsal or ventral components in rats (Kawana and Watanabe 1981; Romanowski et al. 1985; Nicolelis et al. 1995) and primates (Watson et al. 2014), but there are no clear cytoarchitectural boundaries within the mouse ZI. By validating *Th-cre* expression in the ZI, our findings suggest that the mouse ZI contained distinct medial and lateral components, as TH-ir cells were mostly concentrated within the medial ZI and were distinct from cells in the ZIda. The mediolateral distribution of TH-ir ZI cells may

reflect functional differences, as fibers from medial *Th-cre* ZI cells preferentially targeted midline structures (e.g., lateral septum, nucleus of reuniens, posterior hypothalamic nucleus, PAG, SC), while few fibers were laterally distributed in subcortical (e.g., parvicellular part of subparafascicular nucleus or external nucleus of IC) or cortical structures (e.g., central or medial amygdalar nucleus). These projection patterns suggested a medial to lateral conservation of ZI projections, so we predicted that lateral ZI DA cells may preferentially target lateral structures (Kolmac et al. 1998). We can also infer differences in projection patterns of medial and lateral GABAergic ZI cells that preferentially project to rostral and caudal brain regions, respectively, or that have preferential mediolateral or rostrocaudal projections within the same brain region (Yang et al. 2022).

The ZI is important for coordinating defensive (Chou et al. 2018; Lin et al. 2023) and hunting behaviors (Shang et al. 2019; Zhao et al. 2019) in rodents. Indeed, DsRed-labeled fibers were abundant in regions that decrease defensive behaviors to promote hunting, and retrograde tracing studies from these regions, including the PAG (Kolmac et al. 1998), SC (Bolton et al. 2015; Montardy et al. 2022), and LS (LS;Wagner et al. 1995) have corroborated our fiber tracing results. Optogenetic stimulation of PAG-innervating ZI GABA cells decreased flight and freezing behaviors (Chou et al. 2018) and increased the motivation to hunt (Zhao et al. 2019). Therefore, ZI GABA cells may promote hunting by suppressing defensive behaviors (Chou et al. 2018) while promoting motivational drive for feeding (Zhao et al. 2019). Given the critical role of DA in associative learning during emotionally or physically salient events (Bromberg-Martin et al. 2010), it is possible that projections from ZI *Th-cre* cells in the PAG could promote learned associations that facilitate hunting. This would be consistent with previously established roles of the dorsolateral PAG that support memory formation and learned association (Di Scala et al. 1987) via aversive stimuli (Di Scala and Sandner 1989; Castilho and Brandão 2001). The SC is also an important region for coordinating approach (Shang et al. 2019; Huang et al. 2021) and avoidance behaviors (Cohen and Castro-Alamancos 2010; Evans et al. 2018). The SC is functionally divided along its mediolateral axis, where the medial SC promotes defense and avoidance and the lateral SC promotes approach and appetitive behaviors (Comoli et al. 2012). Our DsRed-labeled fibers concentrated toward the midline of the SC; therefore, ZI *Th-cre* projections in the SC may inhibit avoidance behaviors. Finally, the LS is a critical region for regulating defensive and aggressive behaviors, as lesions to this area produce "septal rage" (Bard 1928; Spiegel et al. 1940). Our study revealed dense DsRed-labeled fibers along the border of the dorsolateral LS, which is involved in decreasing fear and freezing responses (Besnard et al. 2019) and preventing the acquisition of fearful memories (Hunsaker et al. 2009; Besnard et al. 2019; Opalka and Wang 2020). ZI *Th-cre* cells may thus regulate the acquisition of fearful memories through the LS. Collectively, ZI *Th-cre* cells densely innervate regions involved in promoting hunting by decreasing defensive behaviors, but the roles of DA within these regions have not yet been defined.

Dopaminergic ZI cells are a unique subpopulation of ZI GABA cells that project to similar downstream targets but also innervate additional brain regions. The MBmot comprised the most projection fibers from ZI DA cells, and this was comparable to that by medial ZI GABA cells (Yang et al. 2022). Similarly, both ZI GABA and DA cells do not project to the cerebellum and only sparsely innervate cortical regions like the striatum and pallidum (Yang et al. 2022). By contrast, medial ZI GABA and DA cells can also display differences in their projection targets. Efferent projections from medial ZI GABA cells were abundant within the sensory–motor cortex-related thalamus (DORsm; Yang et al. 2022), but we found that ZI DA cells preferentially projected to the polymodal association cortex-related thalamus (DORpm). Furthermore, ZI GABA cells send strong projections to the pons (Yang et al. 2022), but our ZI DA cells displayed little or no fibers in the pons. These differences in the distribution of ZI GABA projections suggest that some ZI pathways may function independently of ZI DA cells.

Emerging functions ascribed to ZI DA cells suggested a cooperative relationship with ZI GABA cells to mediate similar outcomes on food- and fear-related behaviors. Optogenetic stimulation of projections from ZI GABA cells in the PVT nucleus elicited robust, binge-like feeding and weight gain (Zhang and van den Pol 2017; Li et al. 2021). Complementing this, chemogenetic activation of ZI DA cells increases the motivation for feeding by increasing meal frequency without increasing overall food intake (Ye et al. 2023). However, as ZI DA cells are also GABAergic (Negishi et al. 2020), the relative contribution of DA and GABA release to control feeding is not known. However, it stands to reason that independent targeting and stimulation of ZI DA and GABA projections at the PVT may elicit synergistic effects that increase the frequency and amount of food intake. Feeding is also regulated by fear, as a hungry animal would not feed in the presence of a predator. The rostral ZI can modulate anxiety-related behaviors (Zhou et al. 2021), and ZI GABA cells contribute by suppressing anxiety-related escape behaviors (Chou et al. 2018) or fear responses (Venkataraman et al. 2021), while ZI DA cells contribute by encoding learned fear associations (Venkataraman et al. 2021). Collectively, ZI GABA and DA cells innervate the same target sites to coordinate similar behaviors, and their coincident outputs may have synergistic outcomes such as those produced during feeding and fear association.

4.1 | Methodological Considerations

Our validation studies revealed a small proportion of ectopic *Egfp* cells that did not express *Th* mRNA or TH immunoreactivity. In our *Th-cre* mice, the *Th* promoter drives the expression of Cre recombinase so that recombination, for example, to produce the *Egfp* reporter in *Th-cre;L10-Egfp* mice, at any period of development would be retained into adulthood. However, *Th* mRNA levels can decrease in adulthood (Bupesh et al. 2014) or fall below detection thresholds, and reduced *Th* gene expression may inadvertently depress TH protein expression.

Additionally, many *Th* mRNA cells did not express TH immunoreactivity, which has been noted before in the hypothalamus (Meng et al. 2018), as well as other brain regions like the olfactory bulbs (Min et al. 1994). Immunodetection of TH protein may be limited by antibody sensitivity or trace TH levels, whose detection at the soma may be facilitated by colchicine pretreatment to disrupt microtubules (Asmus et al. 1992; Asmus and Newman 1993). Nonetheless, cells expressing *Th* mRNA only (i.e., Case 1) had a comparable connectional profile to TH-ir cells (i.e., Case 7), but future work is required

to better understand the developmental trajectory of TH-ir cells in the ZI. At least for DAergic TH cells in the hypothalamus that coexpress other neurotransmitters like GABA (Zhang and van den Pol 2015; Negishi et al. 2020) or glutamate (Meng et al. 2018; Fougère et al. 2021), this mismatch between mRNA and protein expression may signify cells that switch neurotransmitter identity to respond to changes in neuronal activity or emerging stressors (Swanson 1991; Meng et al. 2018). Therefore, while *Th-cre* cells are inherently DAergic, they may produce DA in a state-dependent manner that would be important to consider in behavioral studies.

5 | Conclusion

Overall, medial ZI DA cells have a similar connectivity profile to that of ZI GABA cells, suggesting that ZI DA cells may perform synergistic or opposing functions at the same target sites innervated by ZI GABA cells. Indeed, the studies available demonstrate that ZI DA cells can contribute to nuanced aspects of behaviors attributed previously to ZI GABA cells, including binge-eating, defensive behavior, associated learning, and hunting. We observed the greatest labeling of ZI DA fibers within motor-related regions of the midbrain, particularly within the dorsal PAG and SC. Future work is required to understand the role of DA within these and other downstream targets.

Data Availability Statement

The data that support the findings of this study are available from the corresponding author upon reasonable request.

Peer Review

The peer review history for this article is available at https://publons.com/publon/10.1002/cne.70039

References

Allen Institute for Brain Science 2011. *Technical White Paper: Allen Reference Atlas, Version 1*. Allen Institute for Brain Science.

Asmus, S. E., A. E. Kincaid, and S. W. Newman. 1992. "A Species-Specific Population of Tyrosine Hydroxylase-Immunoreactive Neurons in the Medial Amygdaloid Nucleus of the Syrian Hamster." *Brain Research* 575: 199–207.

Asmus, S. E., and S. W. Newman. 1993. "Tyrosine Hydroxylase mRNA-Containing Neurons in the Medial Amygdaloid Nucleus and the Reticular Nucleus of the Thalamus in the Syrian Hamster." *Brain Research Molecular Brain Research* 20: 267–273.

Bard, P. 1928. "A Diencephalic Mechanism for the Expression of Rage With Special Reference to the Sympathetic Nervous System." *American Journal of Physiology-Legacy Content* 84: 490–515.

Besnard, A., Y. Gao, M. TaeWoo Kim, et al. 2019. "Dorsolateral Septum Somatostatin Interneurons Gate Mobility to Calibrate Context-Specific Behavioral Fear Responses." *Nature Neuroscience* 22: 436–446.

Blomstedt, P., R. Stenmark Persson, G.-M. Hariz, et al. 2018. "Deep Brain Stimulation in the Caudal Zona Incerta Versus Best Medical Treatment in Patients With Parkinson's Disease: A Randomised Blinded Evaluation." *Journal of Neurology, Neurosurgery, and Psychiatry* 89: 710–716.

Bolton, A. D., Y. Murata, R. Kirchner, et al. 2015. "A Diencephalic Dopamine Source Provides Input to the Superior Colliculus, Where D1 and D2 Receptors Segregate to Distinct Functional Zones." *Cell Reports* 13: 1003–1015.

Bono, B. S., N. K. Koziel Ly, P. A. Miller, J. Williams-Ikhenoba, Y. Dumiaty, and M. J. Chee. 2022. "Spatial Distribution of Beta-Klotho mRNA in the Mouse Hypothalamus, Hippocampal Region, Subiculum, and Amygdala." *Journal of Comparative Neurology* 530: 1634–1657.

Bourdy, R., M.-J. Sánchez-Catalán, J. Kaufling, et al. 2014. "Control of the Nigrostriatal Dopamine Neuron Activity and Motor Function by the Tail of the Ventral Tegmental Area." *Neuropsychopharmacology* 39: 2788–2798.

Bouyer, K., and R. B. Simerly. 2013. "Neonatal Leptin Exposure Specifies Innervation of Presympathetic Hypothalamic Neurons and Improves the Metabolic Status of Leptin-Deficient Mice." *Journal of Neuroscience* 33: 840–851.

Bromberg-Martin, E. S., M. Matsumoto, and O. Hikosaka. 2010. "Dopamine in Motivational Control: Rewarding, Aversive, and Alerting." *Neuron* 68: 815–834.

Bupesh, M., A. Vicario, A. Abellán, E. Desfilis, and L. Medina. 2014. "Dynamic Expression of Tyrosine Hydroxylase mRNA and Protein in Neurons of the Striatum and Amygdala of Mice, and Experimental Evidence of Their Multiple Embryonic Origin." *Brain Structure and Function* 219: 751–776.

Castilho, V. M., and M. L. Brandão. 2001. "Conditioned Antinociception and Freezing Using Electrical Stimulation of the Dorsal Periaqueductal Gray or Inferior Colliculus as Unconditioned Stimulus Are Differentially Regulated by 5-HT2A Receptors in Rats." *Psychopharmacology* 155: 154–162.

Chee, M. J. S., P. Pissios, and E. Maratos-Flier. 2013. "Neurochemical Characterization of Neurons Expressing Melanin-Concentrating Hormone Receptor 1 in the Mouse Hypothalamus." *Journal of Comparative Neurology* 521: 2208–2234.

Cheng, H.-Y. M., M. Alvarez-Saavedra, H. Dziema, Y. S. Choi, A. Li, and K. Obrietan. 2009. "Segregation of Expression of mPeriod Gene Homologs in Neurons and Glia: Possible Divergent Roles of mPeriod1 and mPeriod2 in the Brain." *Human Molecular Genetics* 18: 3110–3124.

Chou, X., X. Wang, Z. Zhang, et al. 2018. "Inhibitory Gain Modulation of Defense Behaviors by Zona Incerta." *Nature Communications* 9: 1151.

Choudhury, M. E., T. Moritoyo, M. Kubo, et al. 2011. "Zonisamide-Induced Long-Lasting Recovery of Dopaminergic Neurons From MPTP-Toxicity." *Brain Research* 1384: 170–178.

Chung, E. K. Y., L. W. Chen, Y. S. Chan, and K. K. L. Yung. 2008. "Downregulation of Glial Glutamate Transporters After Dopamine Denervation in the Striatum of 6-Hydroxydopamine-Lesioned Rats." *Journal of Comparative Neurology* 511: 421–437.

Cohen, J. D., and M. A. Castro-Alamancos. 2010. "Neural Correlates of Active Avoidance Behavior in Superior Colliculus." *Journal of Neuroscience* 30: 8502–8511.

Comoli, E., P. Das Neves Favaro, N. Vautrelle, M. Leriche, P. Overton, and P. Redgrave. 2012. "Segregated Anatomical Input to Sub-Regions of the Rodent Superior Colliculus Associated With Approach and Defense." *Frontiers in Neuroanatomy* [Internet] 6: 9. https://www.frontiersin.org/articles/10.3389/fnana.2012.00009.

Diamond, M. E., and E. Ahissar. 2007. "When Outgoing and Incoming Signals Meet: New Insights From the Zona Incerta." *Neuron* 56: 578–579.

Di Scala, G., M. J. Mana, W. J. Jacobs, and A. G. Phillips. 1987. "Evidence of Pavlovian Conditioned Fear Following Electrical Stimulation of the Periaqueductal Grey in the Rat." *Physiology & Behavior* 40: 55–63.

Di Scala, G., and G. Sandner. 1989. "Conditioned Place Aversion Produced by Microinjections of Semicarbazide Into the Periaqueductal Gray of the Rat." *Brain Research* 483: 91–97.

Dong, H. W. 2008. *The Allen Reference Atlas: A Digital Color Brain Atlas of the C57Bl/6J Male Mouse*. John Wiley & Sons Inc.

Evans, D. A., A. V. Stempel, R. Vale, S. Ruehle, Y. Lefler, and T. Branco. 2018. "A Synaptic Threshold Mechanism for Computing Escape Decisions." *Nature* 558: 590–594.

Finley, J. C. W., J. L. Maderdrut, L. J. Roger, and P. Petrusz. 1981. "The Immunocytochemical Localization of Somatostatin-Containing Neurons in the Rat Central Nervous System." *Neuroscience* 6: 2173–2192.

Forel, A. 1877. "Untersuchungen über die Haubenregion und Ihre Oberen Verknüpfungen im Gehirne Des Menschen und Einiger Säugethiere, mit Beiträgen zu den Methoden der Gehirnuntersuchung." *Archiv f Psychiatrie* 7: 393–495.

Fougère, M., C. I. van der Zouwen, J. Boutin, and D. Ryczko. 2021. "Heterogeneous Expression of Dopaminergic Markers and Vglut2 in Mouse Mesodiencephalic Dopaminergic Nuclei A8-A13." *Journal of Comparative Neurology* 529: 1273–1292.

Huang, M., D. Li, X. Cheng, et al. 2021. "The Tectonigral Pathway Regulates Appetitive Locomotion in Predatory Hunting in Mice." *Nature Communications* 12: 4409.

Hunsaker, M. R., G. T. Tran, and R. P. Kesner. 2009. "A Behavioral Analysis of the Role of CA3 and CA1 Subcortical Efferents During Classical Fear Conditioning." *Behavioral Neuroscience* 123: 624–630.

Kawana, E., and K. Watanabe. 1981. "A Cytoarchitectonic Study of Zona Incerta in the Rat." *Journal Fur Hirnforschung* 22: 535–541.

Kolmac, C., and J. Mitrofanis. 1999. "Distribution of Various Neurochemicals Within the Zona Incerta: An Immunocytochemical and Histochemical Study." *Anatomy and Embryology* 199: 265–280.

Kolmac, C. I., B. D. Power, and J. Mitrofanis. 1998. "Patterns of Connections Between Zona Incerta and Brainstem in Rats." *Journal of Comparative Neurology* 396: 544–555.

Krashes, M. J., B. P. Shah, J. C. Madara, et al. 2014. "A Novel Excitatory Paraventricular Nucleus to AgRP Neuron Circuit That Drives Hunger." *Nature* 507: 238–242.

Krimer, L. S., R. L. Jakab, and P. S. Goldman-Rakic. 1997. "Quantitative Three-Dimensional Analysis of the Catecholaminergic Innervation of Identified Neurons in the Macaque Prefrontal Cortex." *Journal of Neuroscience* 17: 7450–7461.

Kuscha, V., A. Barreiro-Iglesias, C. G. Becker, and T. Becker. 2012. "Plasticity of Tyrosine Hydroxylase and Serotonergic Systems in the Regenerating Spinal Cord of Adult Zebrafish." *Journal of Comparative Neurology* 520: 933–951.

Lambe, E. K., L. S. Krimer, and P. S. Goldman-Rakic. 2000. "Differential Postnatal Development of Catecholamine and Serotonin Inputs to Identified Neurons in Prefrontal Cortex of Rhesus Monkey." *Journal of Neuroscience* 20: 8780–8787.

Lepousez, G., Z. Csaba, V. Bernard, et al. 2010. "Somatostatin Interneurons Delineate the Inner Part of the External Plexiform Layer in the Mouse Main Olfactory Bulb." *Journal of Comparative Neurology* 518: 1976–1994.

Li, Y., Z.-W. Liu, G. M. Santana, et al. 2024. "Neurons for Infant Social Behaviors in the Mouse Zona Incerta." *Science* 385: 409–416.

Li, Z., G. Rizzi, and K. R. Tan. 2021. "Zona Incerta Subpopulations Differentially Encode and Modulate Anxiety." *Science Advances* 7: eabf6709.

Lin, C. S., M. A. Nicolelis, J. S. Schneider, and J. K. Chapin. 1990. "A Major Direct GABAergic Pathway From Zona Incerta to Neocortex." *Science* 248: 1553–1556.

Lin, S., M.-Y. Zhu, M.-Y. Tang, et al. 2023. "Somatostatin-Positive Neurons in the Rostral Zona Incerta Modulate Innate Fear-Induced Defensive Response in Mice." *Neuroscience Bulletin* 39: 245–260.

Lindeberg, J., D. Usoskin, H. Bengtsson, et al. 2004. "Transgenic Expression of Cre Recombinase From the Tyrosine Hydroxylase Locus." *Genesis (New York, N.Y.: 2000)* 40: 67–73.

Liu, K., J. Kim, D. W. Kim, et al. 2017. "Lhx6-Positive GABA-Releasing Neurons of the Zona Incerta Promote Sleep." *Nature* 548: 582–587.

Malone, E. F. 1910. "*Über die Kernedes Menschlichen diencephalon.*" Königl. Akademie Der Wissenschaften.

Masri, R., R. L. Quiton, J. M. Lucas, P. D. Murray, S. M. Thompson, and A. Keller. 2009. "Zona Incerta: A Role in Central Pain." *Journal of Neurophysiology* 102: 181.

Meng, D., H.-Q. Li, K. Deisseroth, S. Leutgeb, and N. C. Spitzer. 2018. "Neuronal Activity Regulates Neurotransmitter Switching in the Adult Brain Following Light-Induced Stress." *PNAS* 115: 5064–5071.

Miller, P. A., J. G. Williams-Ikhenoba, A. S. Sankhe, B. H. Hoffe, and M. J. Chee. 2024. "Neuroanatomical, Electrophysiological, and Morphological Characterization of Melanin-Concentrating Hormone Cells Coexpressing Cocaine- and Amphetamine-Regulated Transcript." *Journal of Comparative Neurology* 532: e25588.

Min, N., T. H. Joh, K. S. Kim, C. Peng, and J. H. Son. 1994. "5′ Upstream DNA Sequence of the Rat Tyrosine Hydroxylase Gene Directs High-Level and Tissue-Specific Expression to Catecholaminergic Neurons in the Central Nervous System of Transgenic Mice." *Molecular Brain Research* 27: 281–289.

Montardy, Q., Z. Zhou, L. Li, et al. 2022. "Dopamine Modulates Visual Threat Processing in the Superior Colliculus via D2 Receptors." *Iscience* 25: 104388.

Moon, H. C., and Y. S. Park. 2017. "Reduced GABAergic Neuronal Activity in Zona Incerta Causes Neuropathic Pain in a Rat Sciatic Nerve Chronic Constriction Injury Model." *Journal of Pain Research* 10: 1125–1134.

Nauta, W. J. H., and W. Haymaker. 1969. "Hypothalamic Nuclei and Fiber Connections." In: *The Hypothalamus*, edited by W. Haymaker, E. Anderson, and W. J. H. Nauta. Charles C. Thomas.

Negishi, K., M. A. Payant, K. S. Schumacker, et al. 2020. "Distributions of Hypothalamic Neuron Populations Coexpressing Tyrosine Hydroxylase and the Vesicular GABA Transporter in the Mouse." *Journal of Comparative Neurology* 528: 1833–1855.

Nicolelis, M. A. L., J. K. Chapin, and R. C. S. Lin. 1995. "Development of Direct GABAergic Projections From the Zona Incerta to the Somatosensory Cortex of the Rat." *Neuroscience* 65: 609–631.

Opalka, A. N., and D. V. Wang. 2020. "Hippocampal Efferents to Retrosplenial Cortex and Lateral Septum Are Required for Memory Acquisition." *Learning & Memory (Cold Spring Harbor, New York)* 27: 310–318.

Payant, M. A., C. D. Spencer, N. K. K. Ly, and M. J. Chee. 2024. "Inhibitory Actions of Melanin-Concentrating Hormone in the Lateral Septum." *The Journal of Physiology* 602: 3545–3574.

Paxinos, G., and K. Franklin. 2004. *The mouse brain in stereotaxic coordinates (compact second edition)*. San Diego, USA: Elsevier Science.

Plaha, P., Y. Ben-Shlomo, N. K. Patel, and S. S. Gill. 2006. "Stimulation of the Caudal Zona Incerta Is Superior to Stimulation of the Subthalamic Nucleus in Improving Contralateral Parkinsonism." *Brain* 129: 1732–1747.

Plaha, P., S. Filipovic, and S. S. Gill. 2008. "Induction of Parkinsonian Resting Tremor by Stimulation of the Caudal Zona Incerta Nucleus: A Clinical Study." *Journal of Neurology, Neurosurgery, and Psychiatry* 79: 514–521.

Ramón y Cajal, S. R 1911. "Ramón y Cajal, S. R. (1911/1995)." In *Histology of the Nervous System of Man and Vertebrates*, Translated from the French by N. Swanson and L. W. Swanson. Oxford University Press.

Romanowski, C. A., I. J. Mitchell, and A. R. Crossman. 1985. "The Organisation of the Efferent Projections of the Zona Incerta." *Journal of Anatomy* 143: 75–95.

Shammah-Lagnado, S. J., N. Negrão, and J. A. Ricardo. 1985. "Afferent Connections of the Zona Incerta: A Horseradish Peroxidase Study in the Rat." *Neuroscience* 15: 109–134.

Shang, C., A. Liu, D. Li, et al. 2019. "A Subcortical Excitatory Circuit for Sensory-Triggered Predatory Hunting in Mice." *Nature Neuroscience* 22: 909–920.

Sharma, S., L. H. Kim, K. A. Mayr, D. A. Elliott, and P. J. Whelan. 2018. "Parallel Descending Dopaminergic Connectivity of A13 Cells to the Brainstem Locomotor Centers." *Scientific Reports* 8: 7972.

Simmons, D. M., and L. W. Swanson. 2009. "Comparison of the Spatial Distribution of Seven Types of Neuroendocrine Neurons in the Rat Paraventricular Nucleus: Toward a Global 3D Model." *Journal of Comparative Neurology* 516: 423–441.

Spiegel, E. A., H. R. Miller, and M. J. Oppenheimer. 1940. "Forebrain and Rage Reactions." *Journal of Neurophysiology* 3: 538–548.

Swanson, L. W. 1991. "Biochemical Switching in Hypothalamic Circuits Mediating Responses to Stress." *Progress in Brain Research* 87: 181–200.

Tapia, G. P., L. J. Agostinelli, S. D. Chenausky, et al. 2023. "Glycemic Challenge Is Associated With the Rapid Cellular Activation of the Locus Ceruleus and Nucleus of Solitary Tract: Circumscribed Spatial Analysis of Phosphorylated MAP Kinase Immunoreactivity." *Journal of Clinical Medicine* 12: 2483.

Urbain, N., and M. Deschênes. 2007. "Motor Cortex Gates Vibrissal Responses in a Thalamocortical Projection Pathway." *Neuron* 56: 714–725.

Venkataraman, A., S. C. Hunter, M. Dhinojwala, et al. 2021. "Incerto-Thalamic Modulation of Fear via GABA and Dopamine." *Neuropsychopharmacology* 46: 1658–1668.

Wagner, C. K., M. J. Eaton, K. E. Moore, and K. J. Lookingland. 1995. "Efferent Projections From the Region of the Medial Zona Incerta Containing A13 Dopaminergic Neurons: A PHA-L Anterograde Tract-Tracing Study in the Rat." *Brain Research* 677: 229–237.

Wang, Q., S.-L. Ding, Y. Li, et al. 2020a. "The Allen Mouse Brain Common Coordinate Framework: A 3D Reference Atlas." *Cell* 181: 936–953.e20.

Wang, X., X.-L. Chou, L. I. Zhang, and H. W. Tao. 2020b. "Zona Incerta: An Integrative Node for Global Behavioral Modulation." *Trends in Neuroscience (TINS)* 43: 82–87.

Watson, C., C. R. P. Lind, and M. G. Thomas. 2014. "The Anatomy of the Caudal Zona Incerta in Rodents and Primates." *Journal of Anatomy* 224: 95–107.

Yang, Y., T. Jiang, X. Jia, J. Yuan, X. Li, and H. Gong. 2022. "Whole-Brain Connectome of GABAergic Neurons in the Mouse Zona Incerta." *Neuroscience Bulletin* 38: 1315–1329.

Ye, Q., J. Nunez, and X. Zhang. 2023. "Zona Incerta Dopamine Neurons Encode Motivational Vigor in Food Seeking." *Science Advances* 9: eadi5326.

Zhang, X., and A. N. van den Pol. 2015. "Dopamine/Tyrosine Hydroxylase Neurons of the Hypothalamic Arcuate Nucleus Release GABA, Communicate With Dopaminergic and Other Arcuate Neurons, and Respond to Dynorphin, Met-Enkephalin, and Oxytocin." *Journal of Neuroscience* 35: 14966–14982.

Zhang, X., and A. N. van den Pol. 2017. "Rapid Binge-Like Eating and Body Weight Gain Driven by Zona Incerta GABA Neuron Activation." *Science* 356: 853–859.

Zhao, Z., Z. Chen, X. Xiang, et al. 2019. "Zona Incerta GABAergic Neurons Integrate Prey-Related Sensory Signals and Induce an Appetitive Drive to Promote Hunting." *Nature Neuroscience* 22: 921–932.

Zhou, H., W. Xiang, and M. Huang. 2021. "Inactivation of Zona Incerta Blocks Social Conditioned Place Aversion and Modulates Post-Traumatic Stress Disorder-Like Behaviors in Mice." *Frontiers in Behavioral Neuroscience* 15: 743484.

Supporting Information

Additional supporting information can be found online in the Supporting Information section.